Degradation of OCTG Steel in SAGD Application

by

Ermia Aghaie

A thesis submitted in partial fulfillment of the requirements for the degree of

Master of Science

in

Materials Engineering

Department of Chemical and Materials Engineering

University of Alberta

Abstract

The present research was conducted with the intent of evaluating the degradation of OCTG (Oil Country Tubular Goods) steel used in SAGD (Steam Assisted Gravity Drainage) applications, and developing a promising surface modification method and a novel composite coating using a technique that will have a high possibility of commercialization to improve the corrosion resistance of the OCTG steel in SAGD applications. The corrosion mechanism of OCTG steel in the sour environment consisting of H_2S and CO_2 was fully understood but the performance of the coated (Ni-P coating) and uncoated OCTG steel in a real SAGD operation was not evaluated till now. So in this study, at the first, the coated (electroless Ni-P coating) and uncoated slotted liner used in a real SAGD operation for three months were evaluated by X-ray diffraction (XRD) analysis, field emission scanning electron microscopy (FESEM), energy dispersive spectroscopy (EDS), and optical stereoscopic microscope (OSM) from cross section and surface of the samples. Elemental mapping analysis of the corrosion scale formed on the samples was done from the cross section in order to have a better perspective on performance of the coated and uncoated slotted liner in SAGD operation. Results revealed that applying the Ni-P coating considerably decreased the thickness of the corrosion scale formed on the samples. Also a condensed layer of nickel sulfide formed on the coated samples which can function as a barrier against the diffusion of the corrosive ions from the environment to the substrate. However, the corrosion product formed on the uncoated sample was very porous.

Alloy carbon steel is of great interest in oil sands industry due to its desired strength, flexibility, and low cost. However, the corrosion of this widely used steel in corrosive environments is a great concern. Indeed, finding and applying a promising coating on carbon steel which is used in sour environment (including H_2S and CO_2) have always attracted a significant attention of oil sands industry specifically SAGD industry. The sour environments consisting of H_2S and CO_2 accelerate the corrosion process and degradation of the carbon steel, resulting in replacement of the OCTG in oil sands industry.

As a matter of fact, nitrogen has a substantial effect on the corrosion behavior of steels. In part two of this study, gas nitriding at 850 °C and 950 °C was applied to the carbon steel. The corrosion resistance behavior of the modified samples was investigated by the electrochemical impedance spectroscopy and potentiodynamic polarization tests at the simulated sour environment. After the corrosion test, optical microscope and scanning electron microscopy were employed to evaluate the surface morphology of the samples modified by gas nitriding technique. The results of the polarization testes revealed that the localized corrosion of the carbon steel specimens modified by nitrogen decreased significantly. In addition, the polarization resistance of the carbon steel samples increased considerably after applying the gas nitriding process. However, due to the lack feasibility of using this technique for the industry, I shifted from the gas nitriding to a more applicable technique - electroless plating technique. With this in mind, Ni-P-GO (graphene oxide) composite coating was applied on carbon steel by using electroless plating technique. The electrochemical behavior of the Ni-P-GO was evaluated by potentiodynamic polarization test and EIS in a simulated sour environment saturated by H_2S and CO_2. Morphology, microstructure, elemental analysis, and phase analysis of the coating are investigated by OSM, FESEM equipped with EDS, and X-ray diffraction technique. Microscopic images taken from the Ni-P-GO composite coating revealed that GO nanosheets distributed uniformly through the coating. Electrochemical tests showed that adding graphene oxide nanosheets significantly improved the corrosion resistance of electroless Ni-P coating in the sour environment. Also, results of the EIS test revealed that adding GO nanosheets increased the coating resistance of the electroless Ni-P coating from 1 KΩ.cm^2 to around 12.3 KΩ.cm^2.

Preface

Chapter 1 is the introduction of my research work, including the statement of problem and objectives of my work.

Chapter 2 is the literature review related to my research.

Chapter 3 is the evaluation of the coated (Ni-P electroless coating) and uncoated slotted liner used in a real SAGD operation for some months.

Chapter 4 is the comparisons of L80, Ni-P electroless coating, Ni-P-GO electroless composite coating in the simulated sour environment saturated by H_2S and CO_2 by using electrochemical tests.

Chapter 5 is the comparison of the corrosion resistance of L80 steel and gas nitrided L80 by using electrochemical tests.

Chapter 6 presents the conclusions of my research work.

Chapter 7 includes the recommendations for the further work.

This thesis is dedicated to

My Family

Acknowledgments

I would like to really appreciate my supervisors, Prof. Jing Li Luo and Prof. Hongbo Zeng who supported me and provided me the opportunity to study under their supervision and work on this project. That was a great honor to work with them.

Also, it is a pleasure to appreciate those who made this thesis possible, Dr. Yashar Behnamian, Mr. Michael Leitch, Mr. Brent Fermaniuk, and Mr. Mike Claerhout of RGL Reservoir Management Inc. At the end, thanks to all the technicians and staff members of the Chemical and Materials Engineering (CME) Department.

Table of Contents

List of Tables

List of Figures

List of Symbols

AFM	Atomic Force Microscopy
AE	Alternative Current
CE	Counter Electrode
C_{dl}	Capacitance of Charge Transfer Layer
C_{coat}	Capacitance of Coating
EN	Electroless Nickel
EDS	Energy Dispersive Spectroscopy
EIS	Electrochemical Impedance Spectroscopy
EDS	Energy Dispersive X-ray Spectrometry
FESEM	Field Emission Scanning Electron Microscopy
EC	Equivalent Circuit
E	Potential, V or mV
GO	Graphene Oxide
ID	Inner Diameter
I	Current, A or µA
OCTG	Oil Country Tubular Goods
OSM	Optical Stereoscopic Microscopy
OD	Outer Diameter
OCP	Open Circuit Potential
PD	Potentiodynamic Polarization
RE	Reference Electrode
R	Resistance, $\Omega.cm^2$
R_s	Resistance of Solution, $\Omega.cm^2$
R_{ct}	Charge Transfer Resistance
R_{cot}	Resistance of Coating, $\Omega.cm^2$

SAGD	Steam Assisted Gravity Drainage
SEM	Scanning Electron Microscopy
TEM	Transmission Electron Microscopy
θ	Incident angle in Bragg's Equation, °
WE	Working Electrode
XRD	X-ray Diffraction
Z	Impedance, $\Omega.cm^2$
3-D	Three-Dimensional

Chapter 1: Introduction

1.1 Introduction to SAGD

SAGD stands for steam assisted gravity drainage. SAGD is a technique for extracting the oil from the deep oil sands reservoir. Schematic view of the SAGD operation is demonstrated in Figure 1-1. Roger Butler et al. developed SAGD in 1970s. SAGD is a thermal oil recovery technique, consisting of a pair of two parallel horizontal wells. The top horizontal well is used for steam injection, and the bottom horizontal well is used to collect the extracted fluid which is consisting of brine, clay, sand, and bitumen [1]. The horizontal wells can be placed far above the horizontal production well and close to top of the production well [2]. In SAGD, when the steam chamber is getting bigger, new bitumen is heated and replaced by steam. The heated bitumen has a low viscosity and move downward into a production well by gravity [3]. Over the past ten years, the demand for using this technology in oil sands industry has been increased considerably [4].

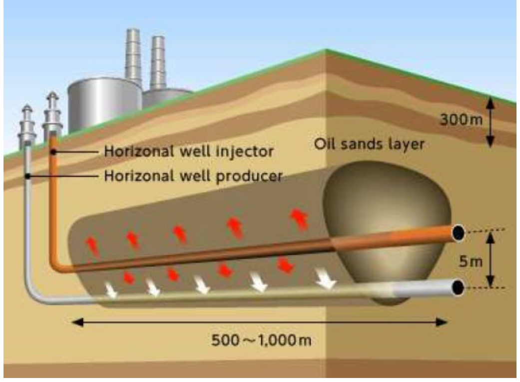

Figure 1-1 Schematic view of the SAGD operation [5].

1.2 Statement of Problem

Oil and gas production environment is where corrosion research is needed the most. It would be due to the criticality of the need to assess the corrosive severity as a means to ensure safe utilization of steels which have a wide application in oil sands industry and SAGD operation. Although CO_2/H_2S corrosion mechanisms have been studied over the past thirty years, precise corrosion prediction does not exist for CO_2/H_2S environments from a stand point of defining limits of use for carbon OCTG steels [6, 7]. In SAGD operation we are dealing with a sour environment consisting of H_2S and CO_2 which accelerates the corrosion process and degradation of the surface metal, resulting in decreasing the production efficiency of the oil or even frequent replacement of the pipeline [8, 9]. The presence of CO_2 and H_2S results in severe corrosion problems in oil and gas pipelines. Indeed, localized corrosion with a high corrosion rate occurs when the corrosion scale does not provide enough protection and is the most frightened type of corrosion attack in oil and gas OCTG [10]. Internal corrosion in wells and pipelines is influenced by temperature, CO_2 and H_2S content, water chemistry, and surface condition of the steel. Alloy carbon steel is of great interest in oil sands industry and SAGD applications due to its desired strength and flexibility, low cost, and good weldability [11], although the corrosion of this kind of steel in corrosive sour environments (consisting of H_2S and CO_2) is a great concern. So, applying a surface modification technique on alloy carbon steel with a high possibility of commercialization would be a great interest for oil sands industry and specifically for SAGD applications.

1.3 Objectives and Scope of My Research

The objective of my research work is to characterize the coated (EN coating) and uncoated pipeline steel used in SAGD (Steam Assisted Gravity Drainage) applications, and also develop a promising surface modification method and a novel composite coating using a technique that will have a high possibility of commercialization to improve the corrosion resistance of the pipeline steel in SAGD applications.

Chapter 2: Literature Review

2.1 Coating

2.2 Electroless Nickel Plating

Electroless coating technique is an autocatalytic chemical reduction process in which the reducing agent is oxidized, resulting in reducing and depositing the nickel ions on the substrate. The first nickel coating layer formed on the substrate acts as a catalyst and facilitates the continuation of the coating process [12, 13]. Electroless coating technique is an appropriate method that can be applied to the complicated shapes, while it would be a big challenge to coat the complicated shapes by using the electrodeposition technique due to various current densities on different parts of the complex shapes [6, 12].

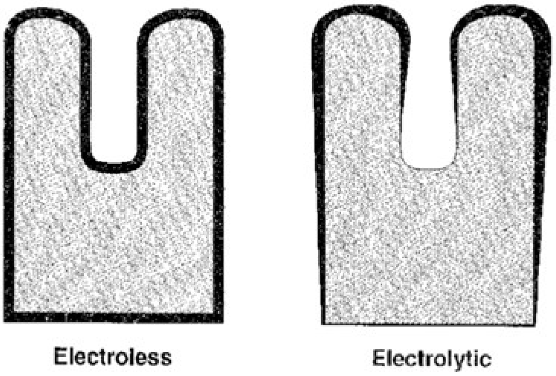

Figure 2-1 Comparing the coating uniformity of electroless and electroplating technique [14].

Electroless nickel coating process can create a very uniform coating on the complicated shapes due to its autocatalytic characteristic. Figure 2-1 demonstrates the advantage of the electroless technique over the electroplating technique [14]. Moreover, electroless technique is capable of coating the both conductive and non-conductive (ceramics and plastics) substrates [12]. Electroless technique has been widely used in various industries due to its excellent physical and mechanical properties [15]. Electroless Ni-P coating is more corrosion resistant in many corrosive environments compared with the pure nickel and chromium coatings [16].

2.2.1. Electroless Ni-P Coating Properties

Electroless Ni-P coating is widely used in various applications due to its excellent characteristics such as high corrosion and wear resistance, appropriate lubrication capability, high hardness, suitable ductility, and soldering capability [12, 13, 17]. Electroless nickel coating that is fabricated by using the hypophosphite reducing agent is considered as a metastable and supersaturated alloy coating [12]. Ni-P coating with less than 7 wt% phosphorous has a crystalline structure, and while the amount of phosphorous exceeds 7 wt%, Ni-P coating has a mixture of amorphous and crystalline structures [18].

2.2.1.1 Mechanical Properties of Electroless Ni-P Coating

Table 2-1 presents the properties of Ni-P coatings according to the phosphorus content in the coating [19].

Table 2-1 Properties of electroless Ni-P coating [19].

Properties	Phosphorous content (%)		
	Low	Medium	High
Phosphorus, % (mass)	1-4	5-8	9-12
Vickers microhardness without heat treatment, HV	650-750	500-550	450-500
Vickers microhardness with heat treatment, HV	1000-1050	900-950	850-900
Melting point, °C	1200	890	870
Density, gr/cm^3	8.5-8.7	8.1-8.3	7.7-7.8
Resistivity, μΩ/cm	50	70	90
Resistance to abrasion	Superior	Very good	Very good
Weldability	Good	Regular	Bad

Heat treatment at 150 °C or 200 °C can improve the coating adhesion. Absorption of hydrogen during the coating process into the high-strength steels that are susceptible to hydrogen embrittlement may result in an unexpected destruction [20]. So, applying the heat treatment process at 200 °C for a few hours can result in the release of hydrogen, decreasing the hydrogen embrittlement susceptibility [20]. The presence of hard particles, the amount phosphorous, and heat treatment process are the three important factors affecting the electroless composite coatings [14, 16]. By increasing the amount hard particles such as SiC and B_4C, the hardness of the Ni-P coating will improve considerably [21].

2.2.1.2 Physical Properties of Electroless Ni-P Coatings

The amount of phosphorous content has a considerable impact on density of the electroless Ni-P coatings [22]. In fact, by increasing the phosphorous content, the coating density is declined

[19]. Electroless nickel coatings are less porous compared to that of produced by electrodeposition technique. The presence of fine particles in electroless composite coatings can suppress the amount of porosities in the coating [22].

2.2.1.3 Corrosion Resistance of Electroless Ni-P Coatings

The important factors that significantly affect the corrosion resistance of electroless Ni-P coatings are as following.

- ✓ Chemical composition and surface properties of the substrate.
- ✓ Surface preparation of the substrate before applying the coating.
- ✓ Coating thickness.
- ✓ Coating porosity.
- ✓ Severity of the corrosive environment.

The amount of phosphorous content substantially affects the corrosion resistance of the electroless Ni-P coatings. Indeed, the corrosion resistance of the electroless Ni-P coatings can be improved by increasing the amount of phosphorous content [15, 23]. Also, adding fine particles can improve the corrosion resistance of the electroless nickel coatings [24]. Using the fine particles such as Si_3N_4, CeO_2, TiO_2, PTFE, and diamond can increase the corrosion resistance of the electroless Ni-P composite coatings [16, 24]. Hong Luo et al. reported that, adding WC nanoparticles improves the corrosion resistance of electroless Ni-P coating in 3.5 wt.% NaCl solution [9].

2.2.2. Electroless Ni-P Coating Applications

The high corrosion resistance, hardness, and wear resistance of the electroless nickel coatings have attracted a great attention of various industries for different applications [19]. Electroless nickel coatings are widely used in oil sands industries. Oil sands equipment are usually exposed to a salty and sour environment consists of CO_2 and H_2S at the temperatures ranging from room temperature up to around 270 °C [7, 19, 25]. In addition, the presence of sand can exacerbate the corrosion problems [7]. Applying the electroless Ni-P coatings with high phosphorous content can substantially improve the performance of the pipeline steel [7, 25]. In fact, using the carbon steel coated by Ni-P coating instead of utilizing stainless steels will result in a great cost saving [7, 19]. Even some stainless steels are coated by electroless nickel coatings in order to prevent the substrate from being corroded in the corrosive environments [7]. Some valves, pipes, oil tanks, and screws used in oil and gas industries are coated by electroless nickel coatings to have a better service performance in the corrosive environments [24]. Electroless Ni-P coating with the phosphorous content of between 9 wt.% and 12 wt.% can be desirable for oil and gas applications exposed to the sour environments [19].

2.3 Composite Coatings

2.3.1. Additives

2.3.1.1 Hard Particles

The hard particles used for electroless nickel composite coatings are usually carbides, diamond, oxides, nitrides, and metallic borides such as chromium, silicon, aluminum, molybdenum, titanium, and tungsten. Some particles such as silicon carbide (SiC), alumina

(Al_2O_3), chromium carbide (Cr_2O_3), titanium carbide (TiC), boron carbide (B_4C), boron nitride (BN), and tungsten carbide (WC) are more applicable in comparison with the other fine particles. Using these particles can significantly improve the hardness, wear resistance, and corrosion resistance of the EN coatings [26-28].

2.3.1.2 Solid Lubricant Particles

Solid lubricant particles are usually spherical with a flat surface. Solid lubricant particles can suppress the friction coefficient of the composite coatings. Solid lubricant particles are usually used at high temperatures, very low temperatures, or in vacuum where the liquid and semi-solid lubricants cannot be used. Some of the commonly used solid lubricant particles are graphite, molybdenum sulfide (MoS_2), tungsten disulfide (WS_2), PTFE, and mica [26, 28].

2.3.1.3 Carbon Nanoparticles and Nanosheets

Carbon nanoparticles have superior characteristics including high hardness, high flexibility, and great lubrication [29]. Using carbon nanoparticles such as carbon nanotubes in electroless Ni-P coatings improves both mechanical and corrosion properties of the coating [29, 30]. Among the various carbon nanoparticles, graphene oxide has superior mechanical and physical properties [16]. Moreover, graphene oxide sheets have a high degree of hydrophilicity due the presence of carboxyl and hydroxyl groups, enabling the graphene oxide sheets to be well distributed in the electroless coating bath [31]. Besides, graphene oxide has a higher corrosion resistance compared with graphene [31]. The presence of carbon nanoparticles in Ni-P coatings can stabilize the electrical double layer, and act as barrier against the diffusion of corrosive ions such as S^-, Cl^-, and HCO_3^- from the environment into the coating and substrate [30, 32, 33]. This concept is schematically demonstrated in Figure 2-2.

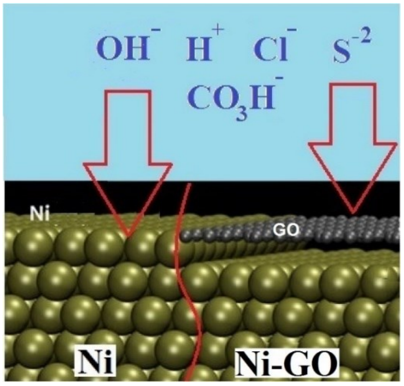

Figure 2-2 Schematic view of the graphene oxide in nickel coating acting as a barrier against the corrosive ions diffusion.

2.3.1.4 Graphene Oxide

Graphene oxide (GO) is a two dimensional material [34]. Chemical structure of graphene oxide is demonstrated in Figure 2-3. Graphene oxide consists of aromatic rings, hydrogenated C (C=C/C-C, C-H), hydroxyl groups (C-OH), epoxy groups (C-O-C), carbonyl groups (C=O), and carboxyl groups (C=O(OH)) [34].

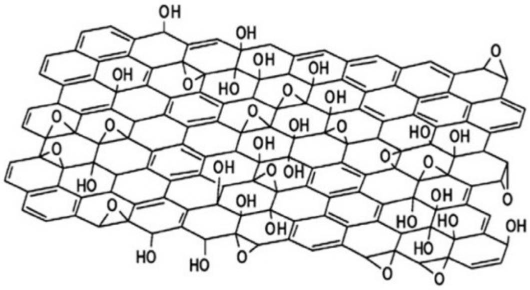

Figure 2-3 Chemical structure of graphene oxide [34].

Due to the presence of some oxygen functional groups, graphene oxide is hydrophilic. So it can be easily dispersed in water. Graphene oxide is chemically very stable [34]. Since the honeycomb hexagonal lattice of GO is disrupted by some functional groups including hydroxyl (OH), carboxyl (COOH), and epoxide (-O-)), GO is an electrical insulator [35]. Schematic view of graphene and graphene oxide is shown in Figure 2-4.

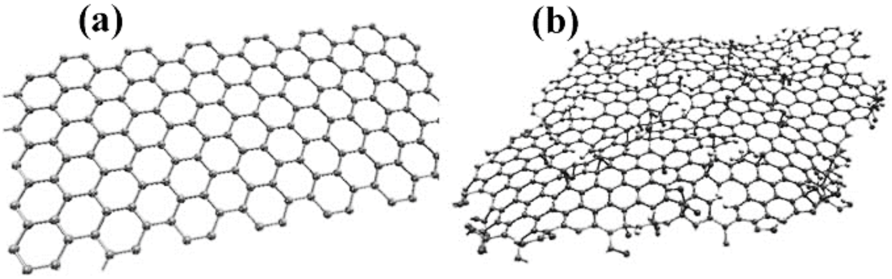

Figure 2-4 Schematic view of graphene (a) and graphene oxide (b) [36].

2.4 Corrosion Resistance of Ni-P Composite Coatings

The corrosion resistance of various electroless Ni-P composite coatings is presented in Table 2-2. As can be seen in Table 2-2, electroless Ni-P-GO (Graphene Oxide) composite coating has the lowest corrosion current among the other kinds of electroless Ni-P composite coatings. Since graphene oxide was discovered just some years ago, only a few works have been done on this kind of superior composite coating. So, Ni-P-GO composite coating can be a great choice to be considered.

Table 2-2 Corrosion resistance of different electroless Ni-P composite coatings.

Type of coating	Method of evaluation	Result	References
Ni-P-Si_3N_4	Potentiodynamic polarization in 3.5% NaCl solution	I_{corr} = 2.5 µA.cm^{-2}	[37]
Ni-P-CeO_2	Potentiodynamic polarization in 3.5% NaCl solution	I_{corr} = 4.0 µA.cm^{-2}	[37]
Ni-P-TiO_2	Potentiodynamic polarization in 3.5% NaCl solution	I_{corr} = 6.0 µA.cm^{-2}	[38]
Ni-P-SiC (40 nm)	Potentiodynamic polarization in 3% NaCl solution	I_{corr} = 2.18 µA.cm^{-2}	[39]
Ni-P-SiC (3 µm)	Potentiodynamic polarization in 3% NaCl solution	I_{corr} = 2.24 µA.cm^{-2}	[39]
Ni-P-SiC (7 µm)	Potentiodynamic polarization in 3% NaCl solution	I_{corr} = 2.15 µA.cm^{-2}	[39]
Ni-P-Al_2O_3 (50 nm)	Potentiodynamic polarization in 3.5% NaCl solution	I_{corr} = 0.96 µA.cm^{-2}	[40]
Ni-P-WC	Potentiodynamic polarization in 3.5% NaCl solution	I_{corr} = 1.0 µA.cm^{-2}	[9]
Ni-P-ZrO_2	Potentiodynamic polarization in 3.5% NaCl solution	I_{corr} = 1.02 µA.cm^{-2}	[41]
Ni-P-SiO_2-Al_2O_3	Potentiodynamic polarization in 3.5% NaCl solution	I_{corr} = 2 µA.cm^{-2}	[42]
Ni-P-ZnO	Potentiodynamic polarization in 3.5% NaCl solution	I_{corr} = 3 µA.cm^{-2}	[24]
Ni-P-$Ni_{3.1}B$	Potentiodynamic polarization in 3.5% NaCl solution	I_{corr} = 3.7 µA.cm^{-2}	[43]
Ni-P-YSZ	Potentiodynamic polarization in 3.5% NaCl solution	I_{corr} = 2.7 µA.cm^{-2}	[44]
Ni-P-BN(h)	Potentiodynamic polarization in 3.5% NaCl solution	I_{corr} = 1.69 µA.cm^{-2}	[45]
Ni-P-SiC-MoS_2	Potentiodynamic polarization in 3.5% NaCl solution	I_{corr} = 1.30 µA.cm^{-2}	[46]
Ni-P-SiC-WS_2	Potentiodynamic polarization in 3.5% NaCl solution	I_{corr} = 1.00 µA.cm^{-2}	[46]
Ni-P-GO (Graphene Oxide)	Potentiodynamic polarization in 3.5% NaCl solution	I_{corr} = 0.18 µA.cm^{-2}	[47]

2.5 Nitriding

Nitriding is a heat treatment process in which nitrogen diffuses into the surface of a metal in order to improve the hardness and corrosion resistance. Nitriding is basically used on low-carbon and low-alloy steels [48]. Nitriding is considered as an important technique for improving the corrosion resistance of carbon steels in corrosive environments [49, 50].

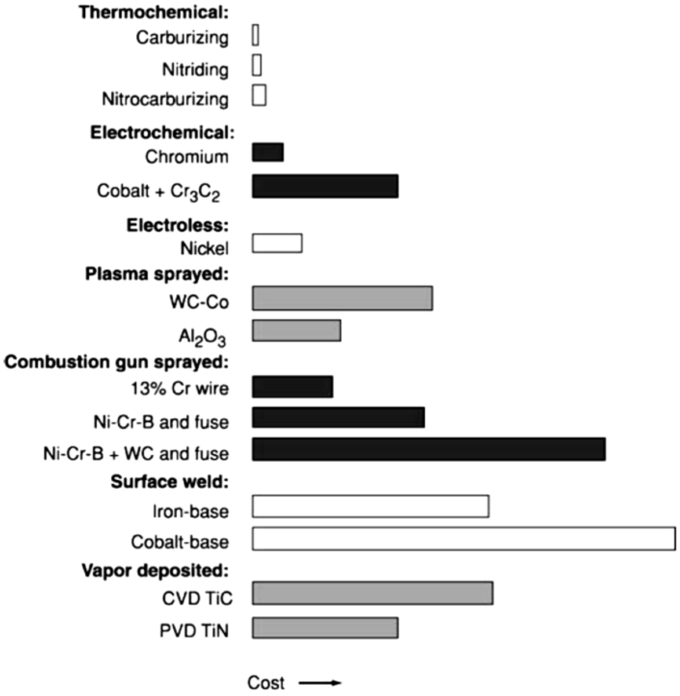

Figure 2-5 Approximate relative costs of various surface treatments [51].

As demonstrated in Figure 2-5, nitriding technique has a lower cost in comparison with the other surface treatment techniques [51]. Also, nitriding can be applied on the complicated shapes [52]. There are three types of nitriding techniques including plasma, salt bath, and gas nitriding [53]. In terms of health hazard and waste disposal problems, required post-treatment process, operating cost, and industrial applicability, gas nitriding is a better option compared with other nitriding techniques [54].

Chapter 3: Evaluating the EN Coating and Coated (Ni-P Electroless Coating) and Uncoated Carbon Steel Used in SAGD Operation

3.1 Introduction

Improving the corrosion resistance of slotted liners in SAGD operation, whose downhole completions equipment must be capable of withstanding a harsh and sour corrosive environment is a great significance for the oil sands industry. Electroless plating technique has attracted a great deal of attention among the various coating techniques due to its simplicity, low cost, very high coating uniformity, and ability to coat complex shapes such as slotted liners [45]. Furthermore, among the various electroless coatings, there is a great interest in using electroless Ni-P coatings due to its excellent corrosion and wear resistance [45]. So, the electroless Ni-P (EN) coating was chosen to improve the performance of the carbon steel in SAGD operation. EN coating was coated on carbon steel slotted liner pipe by using electroless technique. Then, the coated and non-coated carbon steel were used in a real SAGD operation for a few months. The EN coating, and coated (Ni-P electroless coating) and uncoated carbon steel used in SAGD operation were analyzed by using optical stereoscopic microscopy (OSM), scanning electron microscopy (SEM), X-ray diffraction (XRD), and field emission scanning electron microscope (FESEM).

3.2 Sample Preparation

Electroless Ni-P coating was applied on the slotted liner by RGL Reservoir Management Inc. Specification and size of the samples coated with Ni-P is demonstrated in Figure 3-1. Ni-P coating was coated on a slotted liner, then it was cut into some small samples in order to be investigated.

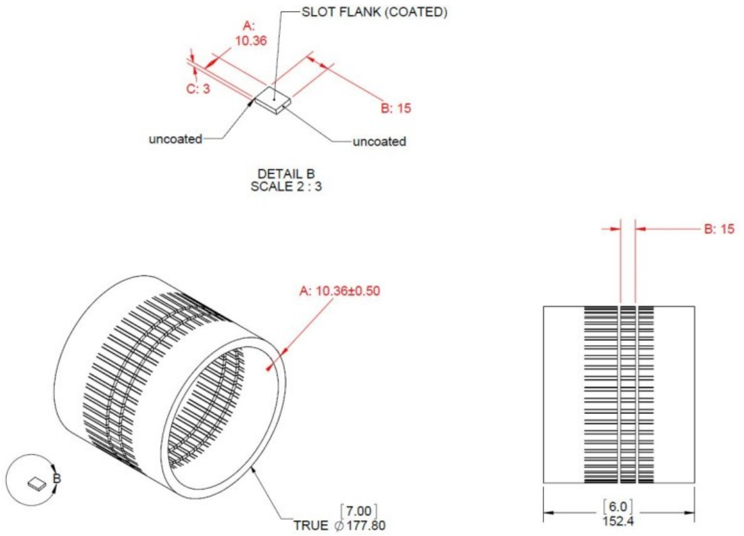

Figure 3-1 Specification and size of the electroless Ni-P coating samples.

The mounted samples were abraded using the silicon carbide paper up to 4000. The prepared sample is demonstrated in Figure 3-2.

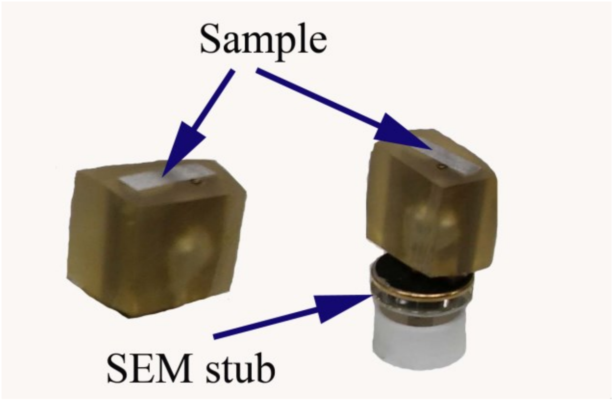

Figure 3-2 The prepared EN coated samples for SEM.

The coated (EN coating) and uncoated carbon steel OCTG were prepared and installed in a tube inside the production well in SAGD operation. Schematic view of the tube in the production well is shown in Figure 3-3.

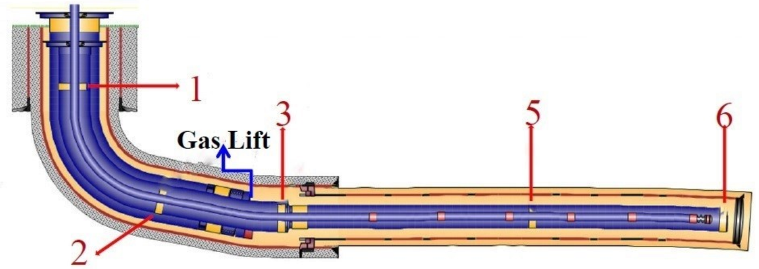

Group / Status	1	2	3	5	6
Coating	A	C	E	G	I
non-coating	B	D	F	H	J

Figure 3-3 Schematic view of the six different locations and the tube inside the production well.

3.3. Characterization

Scanning electron microscope (SEM) equipped with energy dispersive X-ray spectroscopy (EDS) was used to measure the thickness of the EN coating and evaluate the elemental analysis of the coating. Field emission scanning electron microscope (FESEM) (Zeiss Sigma 300 VP) equipped with energy dispersive X-ray spectroscopy (EDS) was employed to evaluate the morphology and the elemental analysis of the corrosion scale of the EN coated and uncoated carbon steel used in SAGD operation for some months. The composition and crystal structure of the corrosion scale of the EN coated and uncoated carbon steel were characterized by X-ray diffraction (XRD) analysis with Cu Kα radiation. Diffraction patterns were recorded in the 2θ range from 10° to 80° at a scanning step of 0.02°. The optical stereoscopic microscopy (OSM) (KEYENCE VHX2000) was used to analyze the surface morphology and topography of the corrosion scale of the samples.

3.4. Results and Discussion

3.4.1. Results of the Ni-P Coating Before Using in SAGD

3.4.1.1. Cross Section Evaluation of EN coating by SEM

In order to measure the thickness of the coating, I have taken some images from the cross section of the coating that are shown in Figure 3-4 and Figure 3-5.

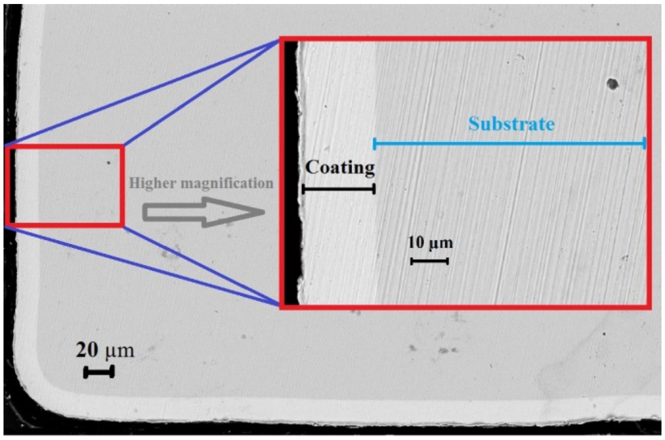

Figure 3-4 SEM cross-section image of the Ni-P coating.

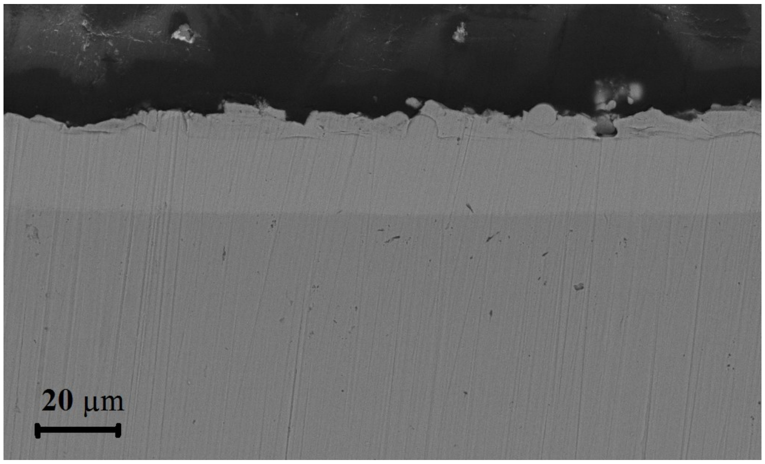

Figure 3-5 SEM cross-section image of the Ni-P coating.

As seen in Figure 3-4, there is a uniform coating through the slot and outside of the pipe, confirming that by using electroless technique we can have a uniform coating on a very complicated shape even through the slot with the width of~ 300 µm. Also no disbanding was observed at the coating-substrate interface.

The coating mechanism consists of anodic (Reaction 3-1) and cathodic (Reaction 3-2) reactions. In anodic reaction, hypophosphite ion reacts with water and produces atomic hydrogen on the surface of the substrate [55].

(3-1)

$$H_2PO_2^- + H_2O \longrightarrow 2H^+ + H_2PO_3^- + 2e^-$$

In cathodic reaction, Ni and P are reduced from Ni^{2+} and hypophosphite ions as shown in Reaction 3-2 [55].

(3-2)

$$H_2PO_2- + 2H^+ + e- \longrightarrow 2H_2O + P$$

$$Ni^{2+} + 2e^- \longrightarrow Ni + 2H^+$$

$$2H^+ + 2e^- \longrightarrow H_2$$

3.4.1.2. EDS Analysis from Cross Section of Ni-P Coating

Energy-dispersive X-ray spectroscopy (EDS) analysis was employed to evaluate the elemental analysis of the EN coating. EDS spectrums of the EN coating (point 1) and carbon steel substrate (point 2) are illustrated in Figure 3-6. During the sample preparation (polishing), just a little amount of iron metal was transported to the coating, so that is why in point 1 a small amount of iron (1.31 atomic percent) was detected.

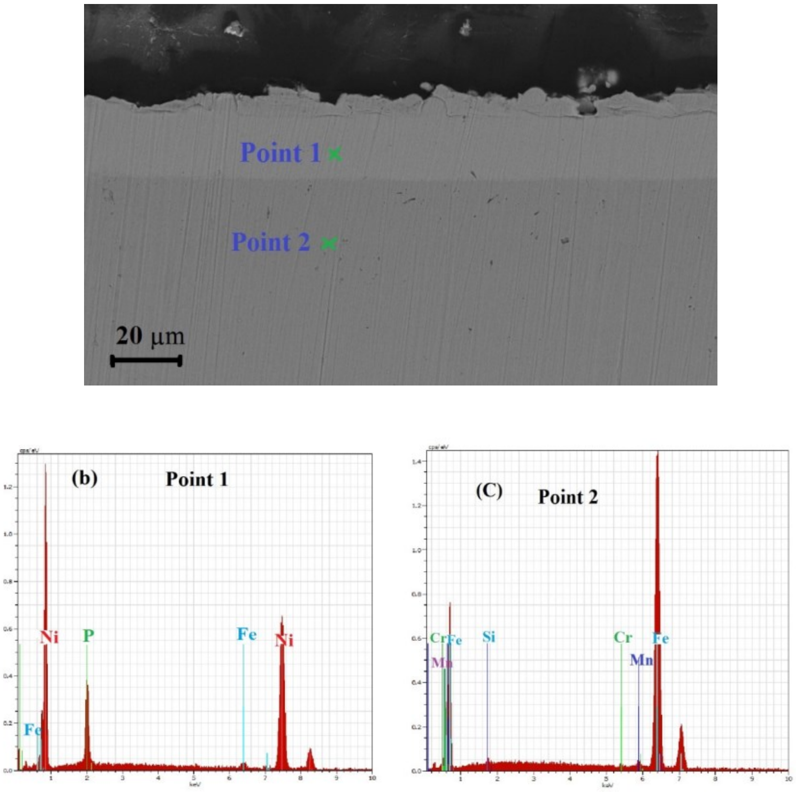

Figure 3-6 SEM cross-section image and EDS spectrum of point 1 (Ni-P coating) and point 2 (substrate).

Quantitative elemental analysis of point 1 (EN coating) and point 2 (substrate) is represented in Table 3-1

Table 3-1 Quantitative EDS analysis of the element proportion of point 1 and 2.

Elements / **Points**	**Nickel** (Wt.%)	**Phosphorous** (Wt.%)	**Iron** (Wt.%)	**Manganese** (Wt.%)	**Chromium** (Wt.%)	**Silicon** (Wt.%)
Point 1	88.71	9.93	1.36	-	-	-
Point 2	-	-	97.33	1.98	0.33	0.36

EDS line scan profile of nickel, phosphorous, and iron along the cross section of the EN coated sample is presented in Figure 3-7.

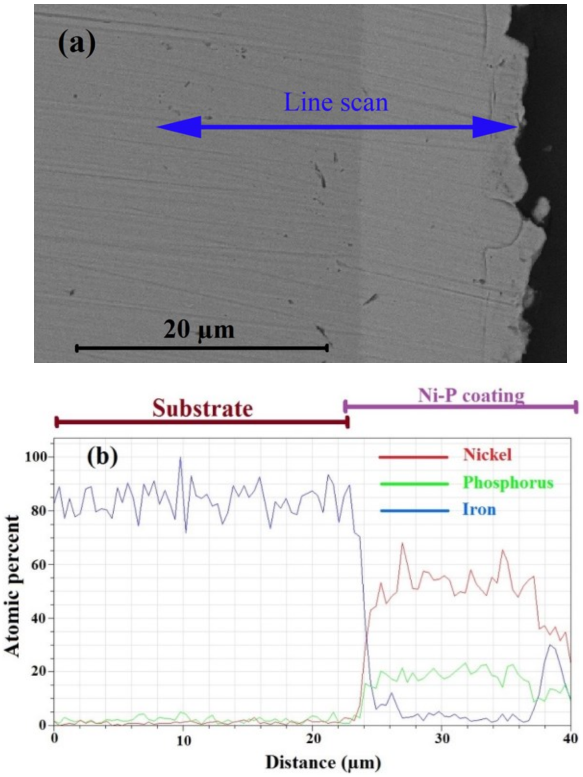

Figure 3-7 SEM and EDS line scan from the cross section of the EN coated sample.

Elemental mapping analysis from the cross section of the Ni-P coating at the microstructural scale by scanning electron microscopy (SEM) equipped with energy dispersive X-ray spectrometer (EDS) is demonstrated in Figure 3-8.

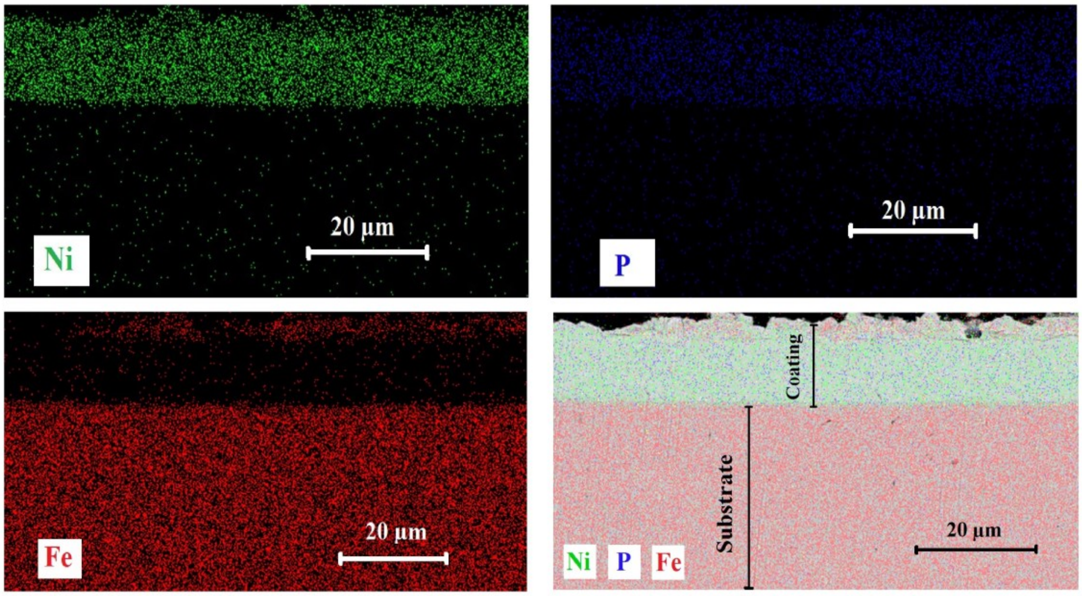

Figure 3-8 EDS mapping image from the cross section of the Ni-P coating.

3.4.2. Results of EN Coated and Uncoated Samples After Using in SAGD

3.4.2.1. Surface Topography

Optical stereoscopic microscope (OSM) was employed to analyze the surface morphology of the coated and uncoated samples. OSM 3-D image taken from the surface of the coated and uncoated samples are presented in Figure 3-9.

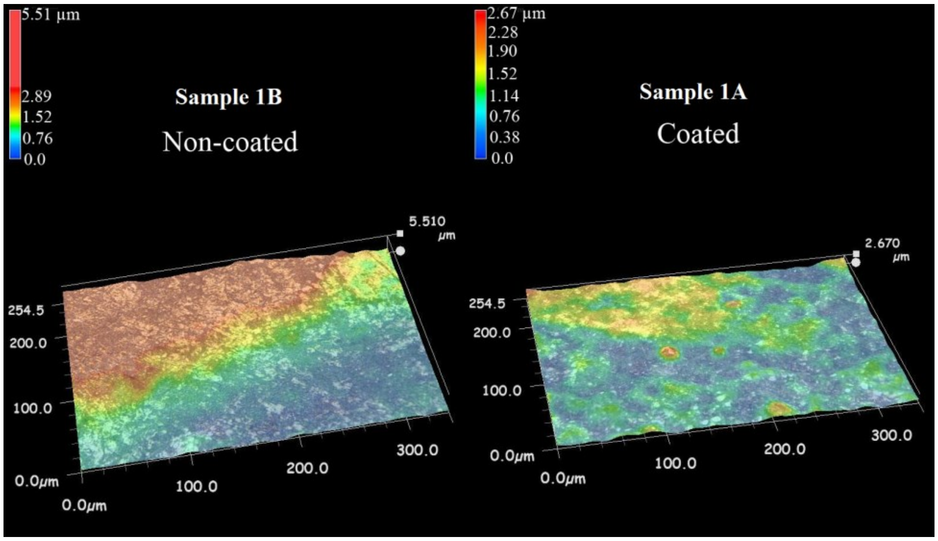

Figure 3-9 OSM 3-D image taken from the surface of the coated (1A) and uncoated (1B) samples used in SAGD operation for some months.

As shown in Figure 3-9, the surface roughness of the coated sample is lower than that of the uncoated one.

3.4.2.2. Cross-Sectional Evaluation of the Corrosion Scale

SEM cross section image taken from the coated and uncoated samples are demonstrated in Figure 3-10.

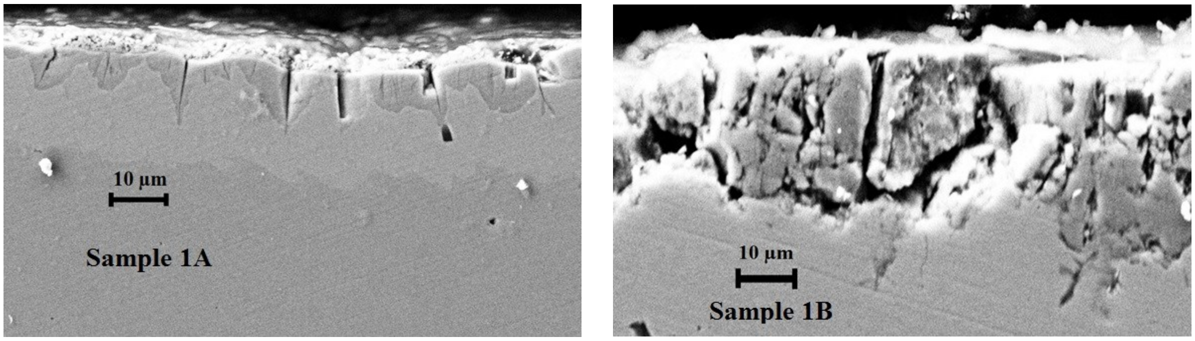

Figure 3-10 SEM cross section image of the sample 1A and 1B.

As illustrated in Figure 3-10, the corrosion product (the scale) from on the uncoated sample (sample 1B) is porous; however, a dense scale formed on the coated sample (sample 1A). Indeed, corrosive ions can diffuse much easier through a porous scale, accelerating the corrosion rate of the substrate. So, the Ni-P coating, significantly improved the corrosion resistance of the carbon steel in SAGD operation. EDS elemental mapping of oxygen for the coated and non-coated sample is shown in Figure 3-11. For the non-coated sample, a thick and porous oxide layer was observed.

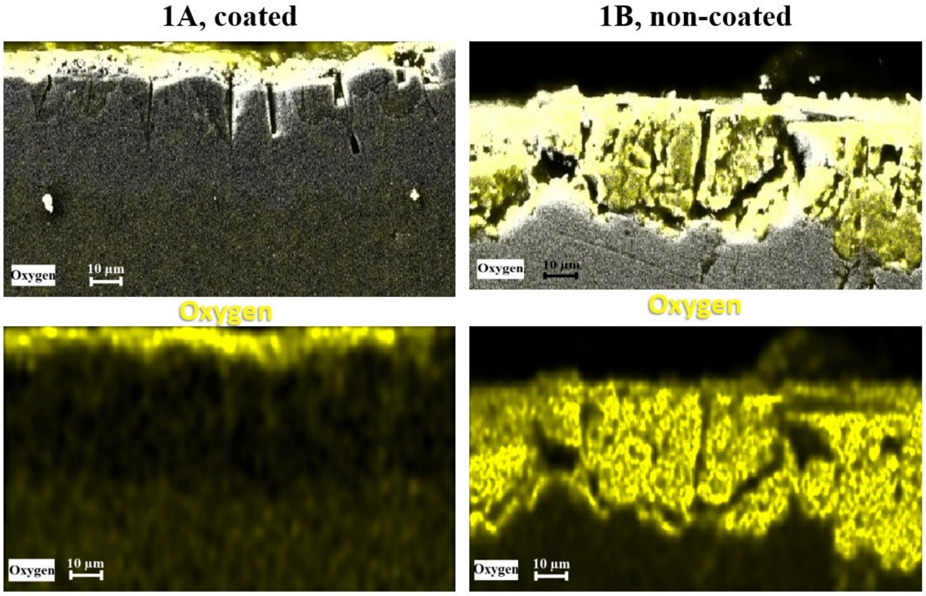

Figure 3-11 EDS elemental mapping of oxygen for the coated and noncoated sample.

Also, for the non-coated sample, the intensity and thickness of the scale consisting of oxygen is much higher than that of the coated one. EDS elemental mapping of carbon and sulfur for the coated and non-coated sample is shown in Figure 3-12.

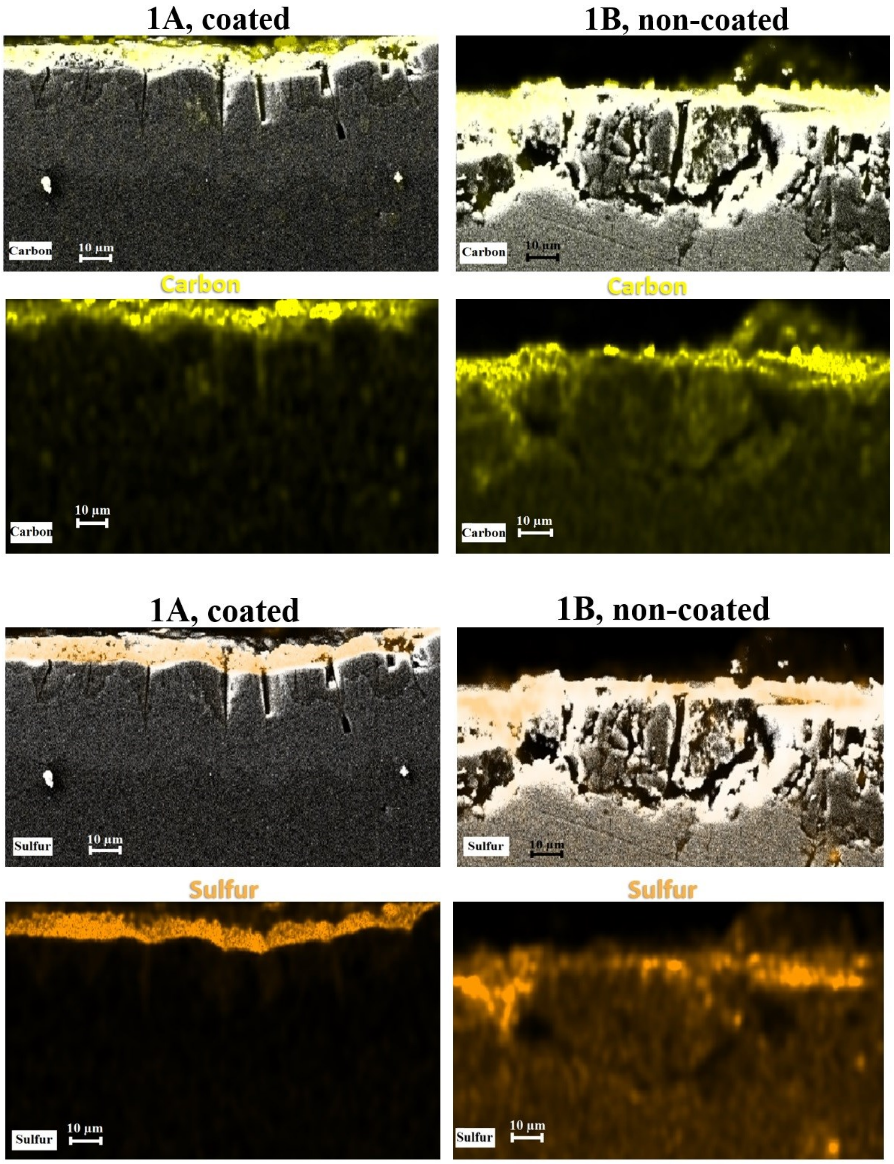

Figure 3-12 EDS elemental mapping of carbon and sulfur for the coated and non-coated sample.

In the non-coated sample, carbon and sulfur diffused through the porous scale. But in the coated sample, a condensed layer of sulfur compound formed on the top of the coating which is functioning as a barrier against the corrosive environment and significantly increases the corrosion resistance. Figure 3-13 illustrates the EDS elemental mapping of nickel and phosphorus for the coated sample (1A).

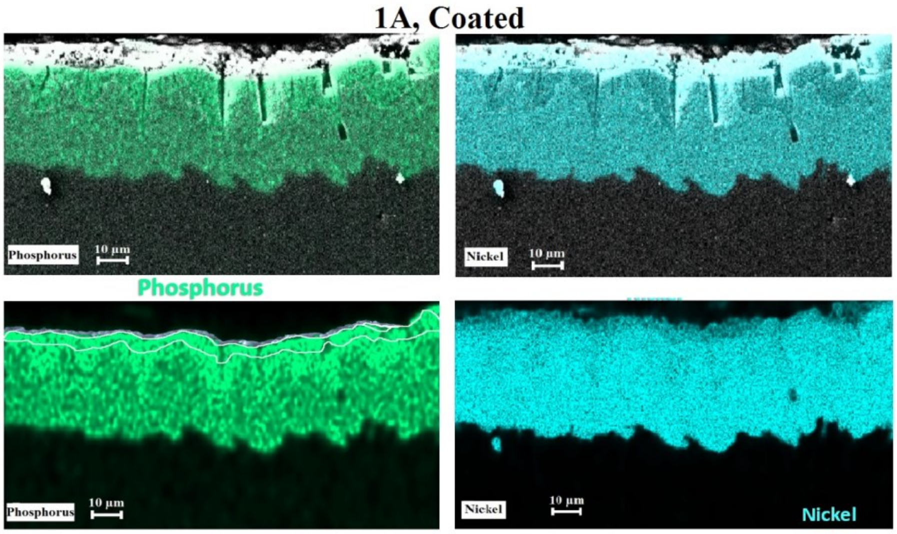

Figure 3-13 EDS elemental mapping of nickel and phosphorus for the coated sample (1A).

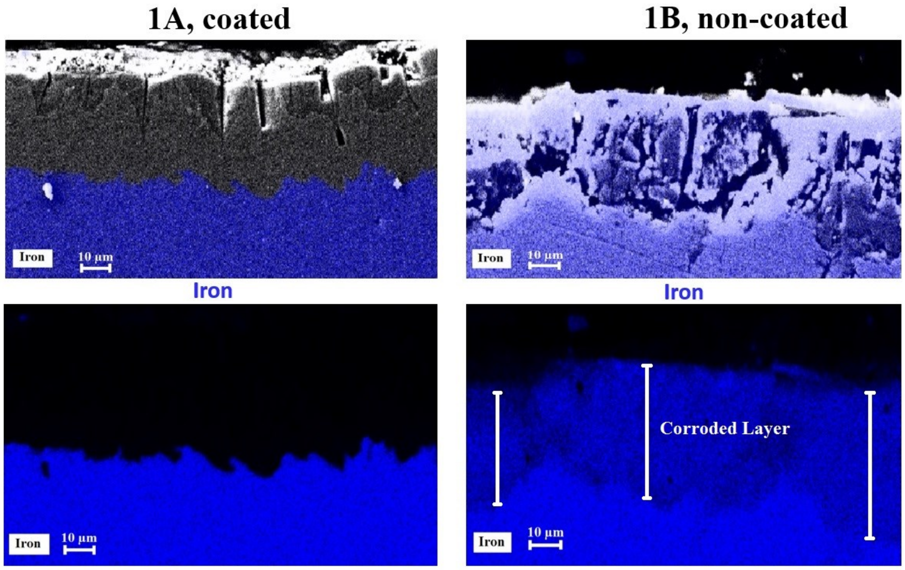

Figure 3-14 EDS elemental mapping of iron for the coated (1A) and non-coated (1B) sample.

EDS elemental mapping of iron for the coated (1A) and non-coated (1B) sample is revealed in Figure 3-14. The blue color shows the presence of the iron.

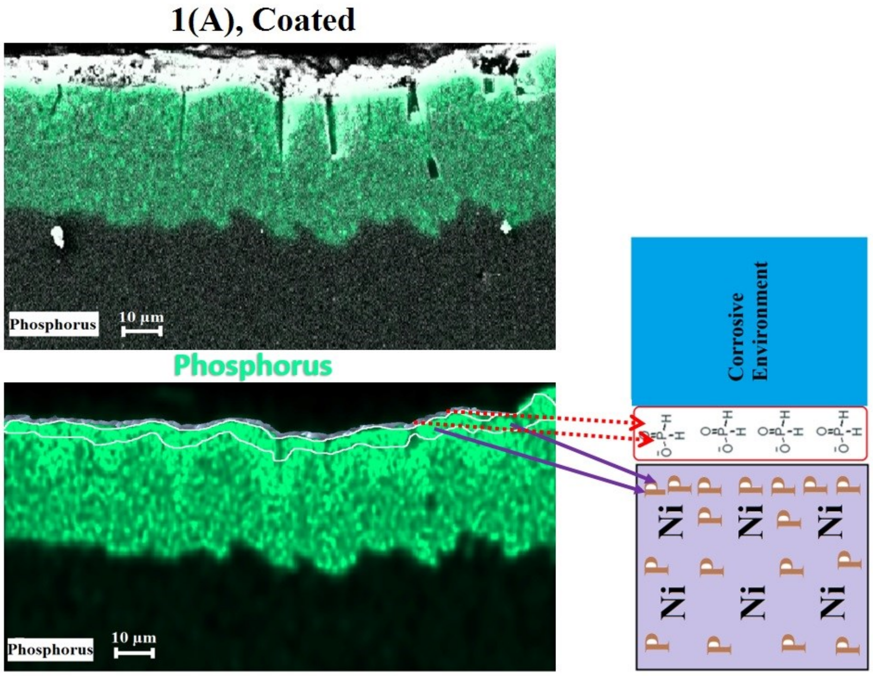

Figure 3-15 Schematic view of the general corrosion mechanism of Ni-P coating.

Figure 3-15 shows the schematic view of the general corrosion mechanism of Ni-P coating. In fact, nickel is preferentially dissolved from the Ni-P coating at a certain potential, leading to the enrichment of phosphorus on the surface layer. The layer enriched by phosphorus reacts with water and forms a layer of hypophosphite anions. This hypophosphite anions layer can block the supply of water to the electrode surface, which is thereby preventing the hydration of nickel [56].

3.4.2.3. X-Ray Diffraction Analysis of the Corrosion Scale

X-ray diffraction (XRD) analysis was employed in order to evaluate the composition of the corrosion scale of the EN coated and uncoated samples. Figure 3-16 illustrates the XRD patterns of the corrosion scale of the coated sample (sample 1A) that used in SAGD operation for some months.

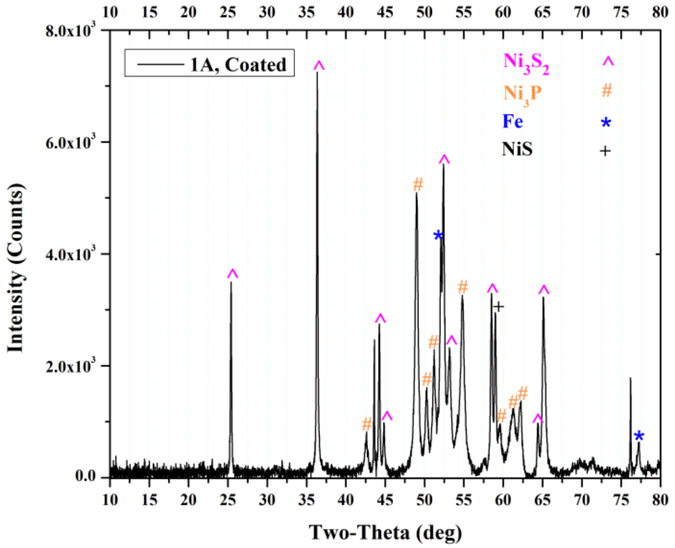

Figure 3-16 X-ray diffraction patterns of the EN coated (1A) sample.

XRD results of the corrosion scale of the coated sample confirmed the formation of some condensed nickel sulfide compounds such as NiS and Ni_3S_2. The nickel sulfide layer formed on the top of the Ni-P coating acts a protective layer against the corrosive environment [57]. X-ray diffraction patterns of the uncoated (1B) sample is demonstrated in Figure 3-17. It shows the composition (Fe_2O_3, FeS, and Fe_3O_4) of the scales formed on the OCTG carbon steel which used in SAGD operation for some months.

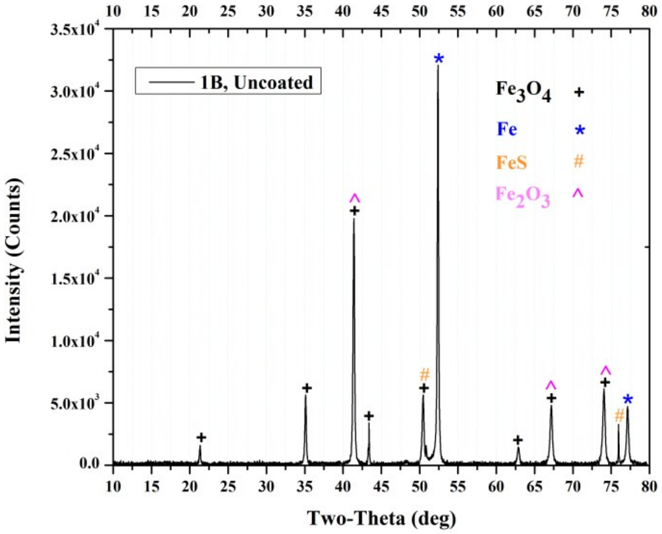

Figure 3-17 X-ray diffraction patterns of the uncoated (1B) sample.

The main anodic and cathodic reactions of the EN coated and non-coated samples in the sour environment in SAGD are demonstrated in

Table 3-2. The main reactions at anode and cathode in the sour environment

	Anode	Cathode
EN coated sample	$H_2S \longrightarrow H^+ + HS^-$ $HS^- \longrightarrow H^+ + HS^{2-}$	$Fe \longrightarrow Fe^{2+} + 2e^-$ $Fe^{2+} + S^{2-} \longrightarrow FeS$
Non-coated sample	$H_2S \longrightarrow H^+ + HS^-$ $HS^- \longrightarrow H^+ + HS^{2-}$	$3Ni + S^{2-} \longrightarrow Ni_3S_2$

3.5. Conclusions

The electroless Ni-P coating significantly improved the corrosion resistance of the slotted liner made of carbon steel. EDS elemental analysis from the cross section and XRD results from the corrosion scales of the EN coated sample revealed the formation of a condensed layer of nickel sulfide including NiS and Ni_3S_2, acting as a barrier against the corrosive sour environment. The nickel sulfide layer formed on the top of the EN coated sample is a protective layer against the corrosion. Also, XRD results showed the presence of a stable intermetallic phases (such as Ni_3P) in the OCTG steel coated by EN coating. The scale formed on the uncoated OCTG steel was more porous in comparison with the scale formed on the EN coated OCTG steel.

Chapter 4: Improving the Corrosion Resistance of Carbon Steel in Sour Environment by Electroless Ni-P-GO Composite Coating

4.1. Introduction

Electroless plating technique has attracted a great deal of attention among the various coating techniques because of its significant characteristics including simplicity, low cost, and high uniformity of the deposits even on the complicated shapes [22, 57, 58]. In addition, among the various electroless coatings, there is a great interest in using Ni-P coatings in various oil sands industry for the sake of its high corrosion resistance and wear resistance [19, 59]. Improving the corrosion resistance of electroless Ni-P coatings by adding nanoparticles such as oxides and carbides particles considerably enhanced the use of this coating in the extremely high corrosive environments [37, 60, 61]. Indeed, the presence of just a few percent of ceramic nanoparticles in Ni-P coating can substantially improve its corrosion and wear behavior in the corrosive environments consist of hydrogen sulfide and carbon dioxide [62, 63]. Ni-P coating reinforced by carbon nanomaterials such as carbon nanotubes, graphene, and graphene oxide is of great significance due to the superior characteristics of carbon nanomaterials [30, 64]. Using carbon nanosheets such as graphene and graphene oxide significantly improves the corrosion resistance of Ni-P coatings [16, 64]. Dedkov et al. [66] reported that, graphene can substantially enhance the corrosion resistance of Ni-P coating since the graphene sheets imbedded inside the coating act as barrier against the diffusion of the corrosive agents. Graphene oxide is much more chemically stable in electrochemical reactions compared to graphene because of its oxygen-carbon bonds [31, 66]. In fact, graphene oxide sheets as the promising component in Ni-P-GO (graphene oxide) composite coating can further improve the corrosion resistance of the coating against the corrosive environments [31, 66].

In this study, single-layer graphene oxide sheets were used to produce Ni-P-GO composite coating by using electroless technique. Field emission scanning electron microscope (FESEM) and X-ray diffraction (XRD) analysis were employed to evaluate the effect of the presence of the graphene oxide on morphology and phase analysis of the Ni-P-GO composite coating, respectively. In order to investigate the impact of the presence of the graphene oxide sheets on electrochemical behavior of the Ni-P coating, electrochemical impedance spectroscopy and polarization tests were conducted in sour environment in accordance with the NACE TM0177-96 standard.

4.2. Materials and Method

Ni-P coating and Ni-P-GO composite coating was coated on L80 carbon steel substrate by using electroless technique. L80 carbon steel specimens as the substrate were cute into 10mm×10mm×10mm, and polished by SiC grinding papers ranging from very coarse 200 grit to very fine 2500 grit sizes. Later on, specimens were washed by alcohol in ultrasonic bath for 15 min. The surface was then cleaned with 10% sodium hydroxide (NaOH) at 70-80 ºC for 4-5 min. Afterwards, in order to activate the surface, specimens were immersed in into 5 wt.% hydrochloric acid for 0.5-1 min, then rinsed with distilled water and dried. The bath composition and electroless plating parameters are illustrated in Table 4-1. Single layer GO nanosheets were added to the coating bath and stirred by ultrasonic stirrer for around 2 hours. Then, the coating bath was heated up to 85 ºC and the specimen was immersed in the bath for 2 hours for deposition. During the deposition process, the coating bath was stirred by a magnetic stirrer with the rate of 250 rpm and temperature of the bath was kept constant at 85 ºC by using a heater. After deposition, specimens were immersed in an alcohol solution for a few min, exposed to an ultrasonic bath cleaner.

Table 4-1 Bath composition and electroless plating parameters for Ni-P-GO composite coating.

Deposition parameters	**Amount**
$NiSO_4 \cdot 6H_2O$	20-30 $g.L^{-1}$
$NaH_2PO_2 \cdot H_2O$	20-30 $g.L^{-1}$
Sodium acetate	10-15 $g.L^{-1}$
Citric acid	15-20 $g.L^{-1}$
Pb^{+2}	2 $mg.L^{-1}$
Lactic acid	15-20 $ml.L^{-1}$
Graphene oxide	40 $mg.L^{-1}$
Temperature	85 ± 1 °C
pH	5.5-7.5
Agitation	250 rpm
Time	120 min

After the coating process, morphology and elemental analysis of the specimens were investigated by field emission scanning electron microscope (FESEM) (Zeiss Sigma 300 VP) equipped with energy dispersive X-ray spectroscopy (EDS) analysis. A Rigaku Ultima IV X-ray diffractometer (XRD) was used to study the crystal structure of the coatings. Transmission electron microscope (TEM) analysis and electron energy loss spectroscopy (EELS) mapping analysis was used to characterize GO nanosheets. Electrochemical behavior of the L80 carbon steel, Ni-P coating, and Ni-P-GO composite coating in a sour environment prepared according to the NACE TM0177-96 was investigated by a Gamry system potentiostat/frequency response analyzer (model 1260A). The corrosion test solution was consisted of 5.0 wt% NaCl and 0.2 wt% acetic acid dissolved in deionized water with the pH of ~ 4. The test solution was deaerated by purging an inert gas at a rate of at least 100 mL/min for at least 1 h/L of solution. Then, the test solution was saturated with H_2S and CO_2 by purging these two gases at a rate of at least 100 mL/min for at least 20 min/L of test solution. The corrosion test setup for the simulated sour environment is shown in.

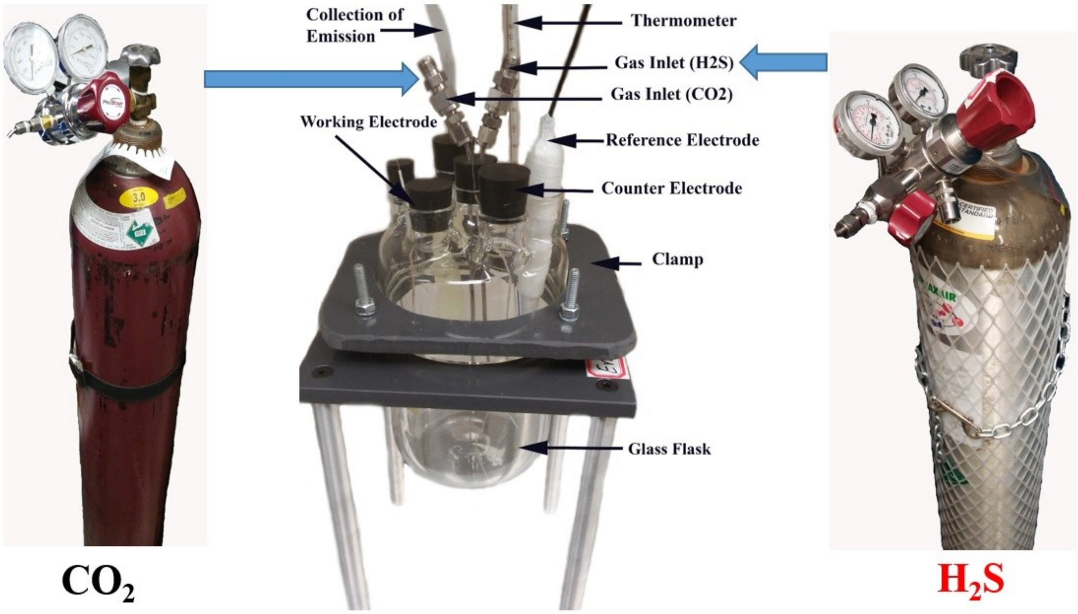

Figure 4-1 The corrosion test setup for the simulated sour environment.

demonstrates the prepared coating setup for electroless Ni-P and Ni-P-GO composite coating.

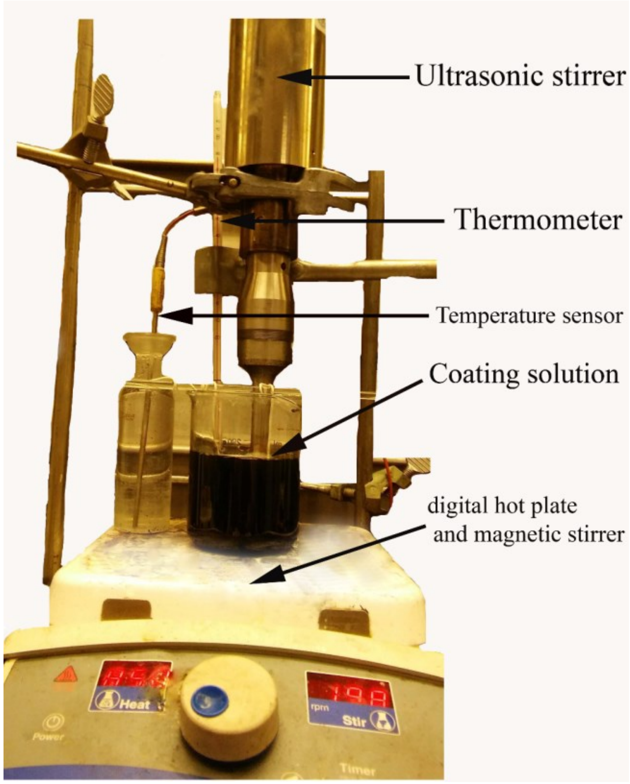

Figure 4-2 The prepared coating setup for the electroless Ni-P and Ni-P-GO composite coating.

Also, the schematic view of the coating setup is shown in Figure. The coated or uncoated L80 carbon steel was the working electrode, the platinum electrode was the counter electrode, and the saturated calomel electrode (SCE) was the reference electrode. Prior to electrochemical tests, specimens were put in the corrosion solution for 1 hour in an open circuit potential (OCP) in order to reach a steady-state potential. Polarization tests were conducted with a scan rate of 1 mV/s from 500 mV lower than OCP to 500 mV above the OCP.

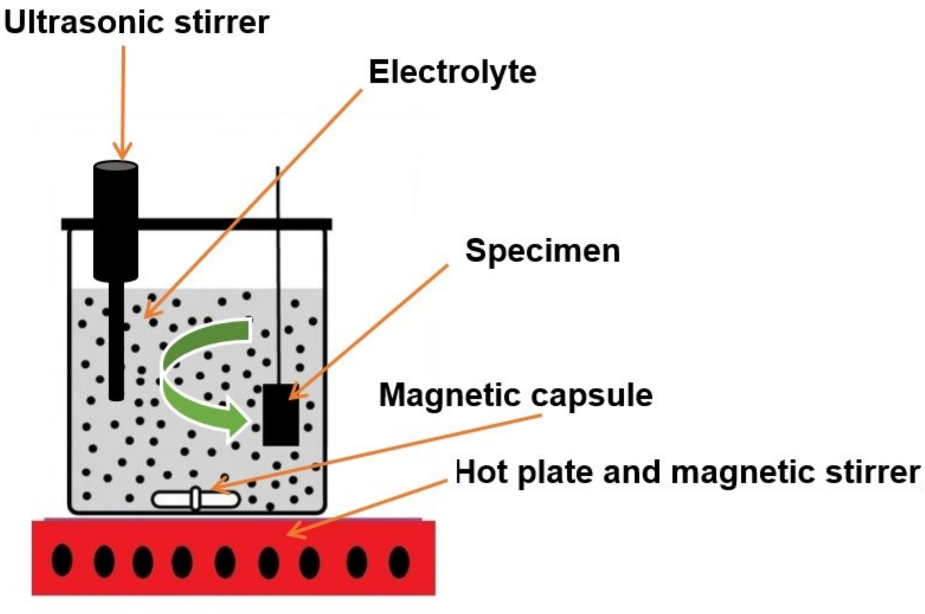

Figure 4-3 Schematic view of the coating setup.

Electrochemical impedance spectroscopy test was performed in OCP at the frequency ranging from 100 kHz to 10 mHz, with the applied potential of 10 mV. After the corrosion tests, surface morphology of the corroded specimens was evaluated by FESEM.

4.3. Results and Discussion

Figure 4-4 demonstrates TEM image and EELS mapping analysis of the graphene oxide.

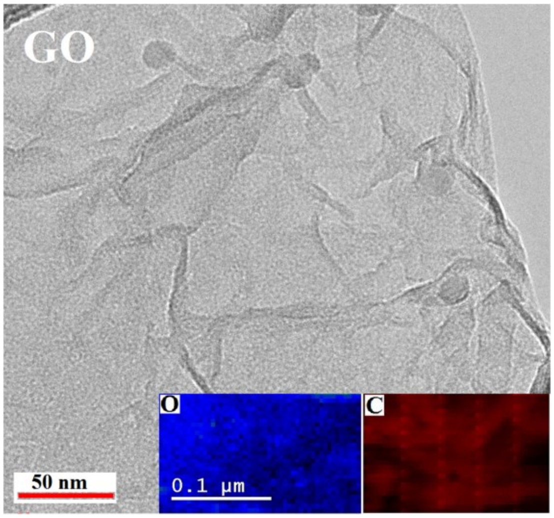

Figure 4-4 TEM image and EELS mapping of the graphene oxide.

As shown, carbon and oxygen distributed uniformly through the graphene oxide sheet. The AFM images of the GO at two different magnifications along with the roughness profile are demonstrated in Figure 4-5. As shown in Figure 4- (B), GO sheet nano-layers can be readily recognized in the surface topography image.

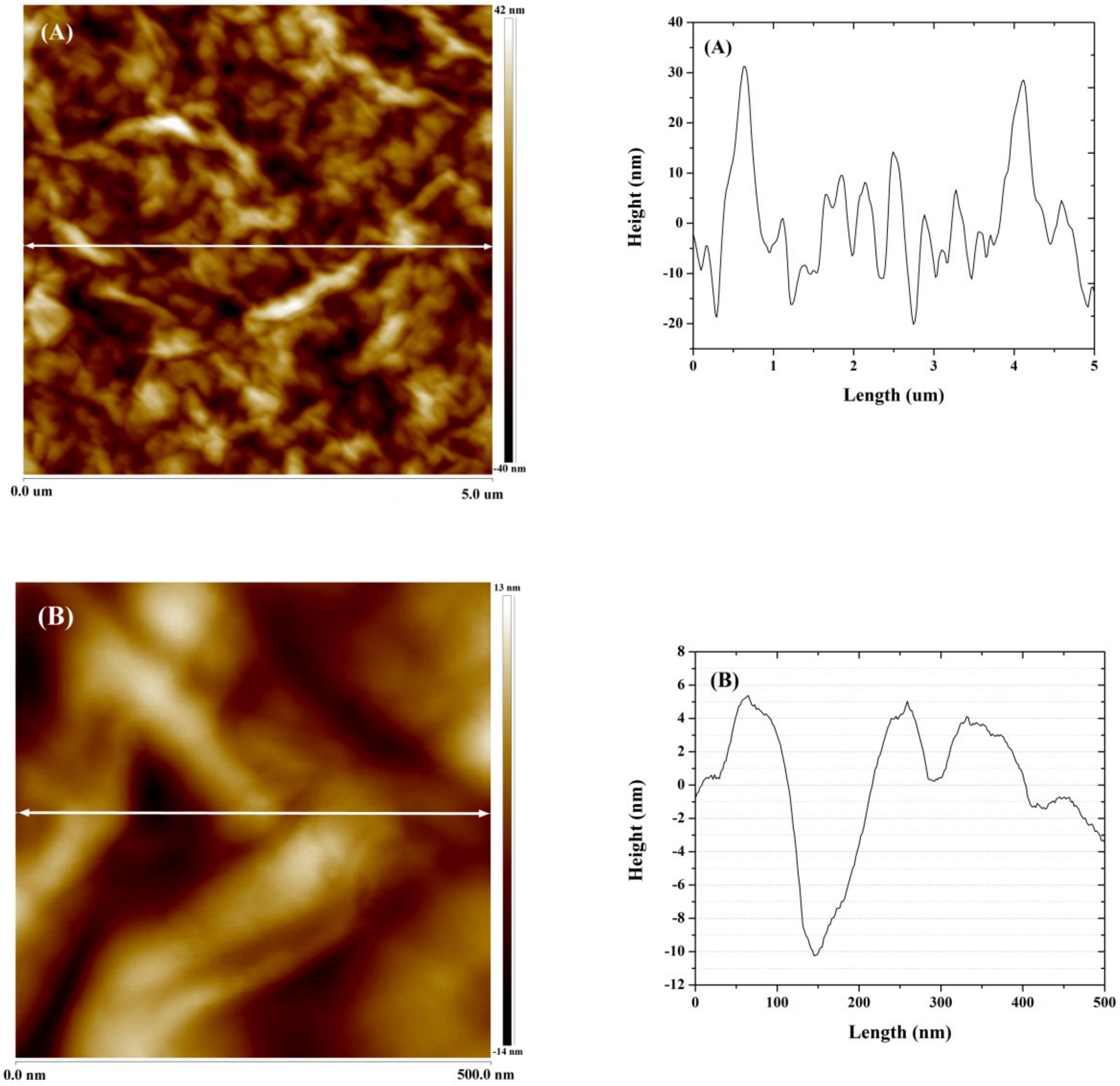

Figure 4-5 AFM images of the GO at two different magnifications along with the roughness profile.

XRD pattern of the Ni-P-GO composite coating and Ni-P coating are illustrated in Figure 4-6.

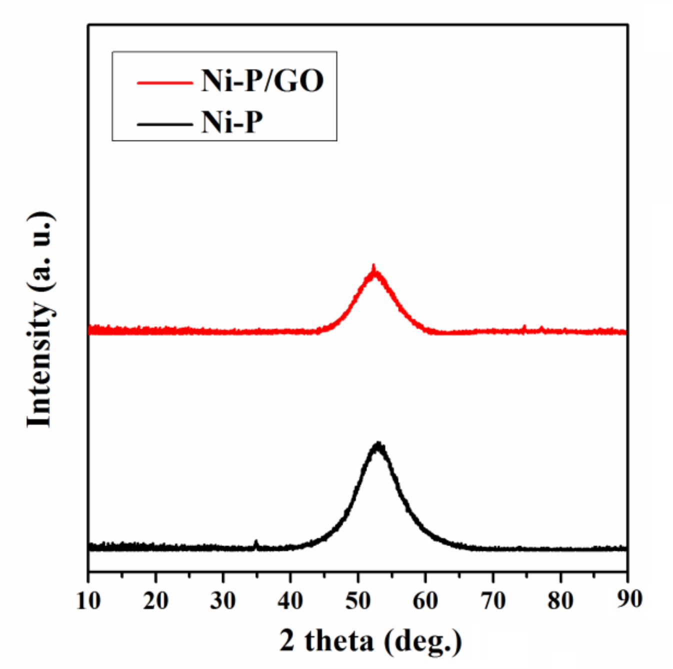

Figure 4-6 X-ray diffraction patterns of Ni-P coating and Ni-P-GO composite coating.

Figure 4-7 illustrates FESEM images of the Ni-P coating (a and c) and Ni-P-GO composite coatings (b and d). As can be seen, graphene oxide sheets are well distributed among the Ni-P grains. Graphene oxide sheets are shown by arrow in Figure 4-6 (d). GO sheets has a high surface energy [68]. By adding GO nanaosheets to the coating solution, there will be more nucleation sites for the Ni-P coating to initiate. So the grain size of the Ni-P coating will decrease. As demonstrated in Figure 4-6, after adding GO sheets to the coating, the X-ray diffraction peak of the coating was broadened, representing the fact that grain size was reduced [69].

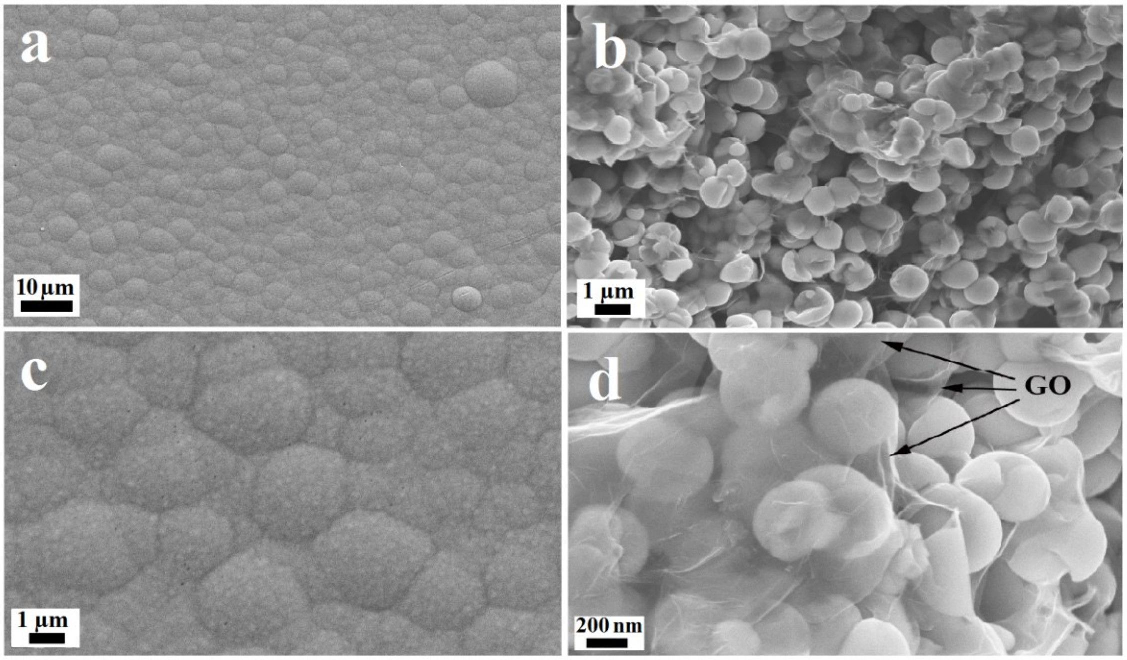

Figure 4-7 FESEM images of the Ni-P coating (a and c) and Ni-P-GO composite coatings (b and d).

By evaluating the surface morphology, it can be represented that, using graphene oxide sheets resulted in a relatively uniform distribution of the Ni-P grains, and also the grain size was decreased. The elemental mapping analysis of the Ni-P-GO composite coating is represented in Figure. The relatively uniform distribution of carbon and oxygen in Figure 4-8 reveals that graphene oxide sheets are well distributed in the coating. Figure 4-9 reveals the EDS elemental mapping analysis of the electroless Ni-P coating. As see, nickel and phosphorous distributed uniformly through the coating.

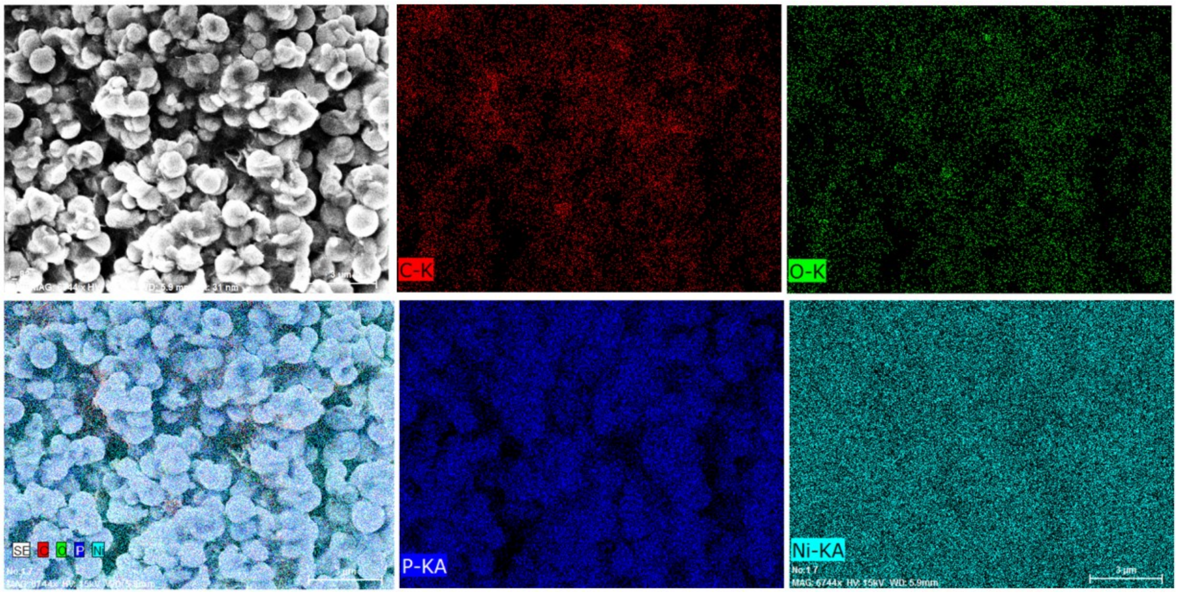

Figure 4-8 EDS elemental mapping analysis of the Ni-P-GO composite coating.

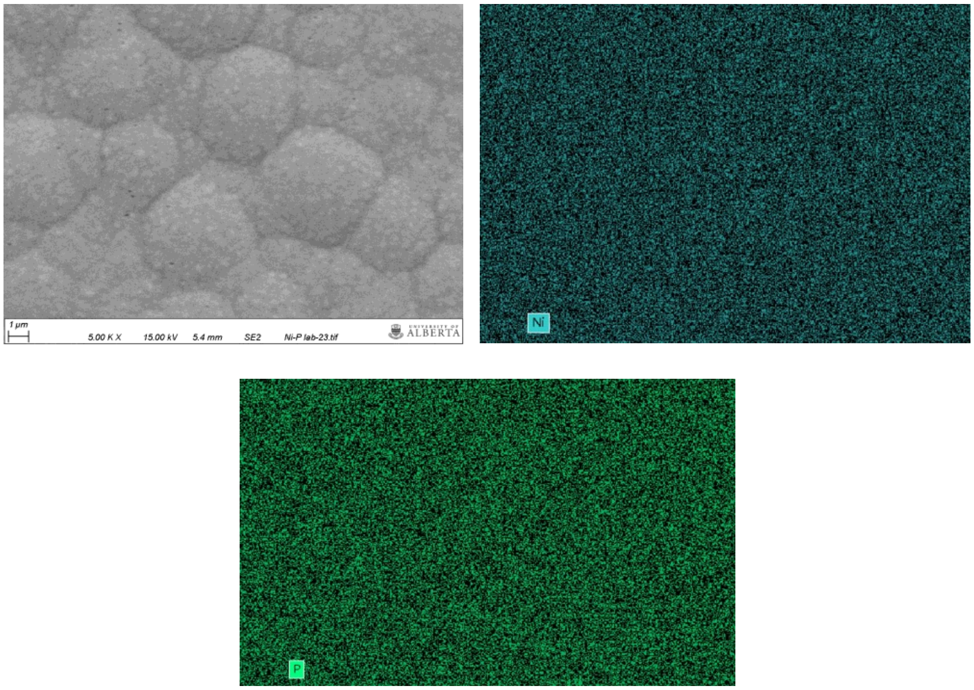

Figure 4-9 EDS elemental mapping analysis of the Ni-P coating.

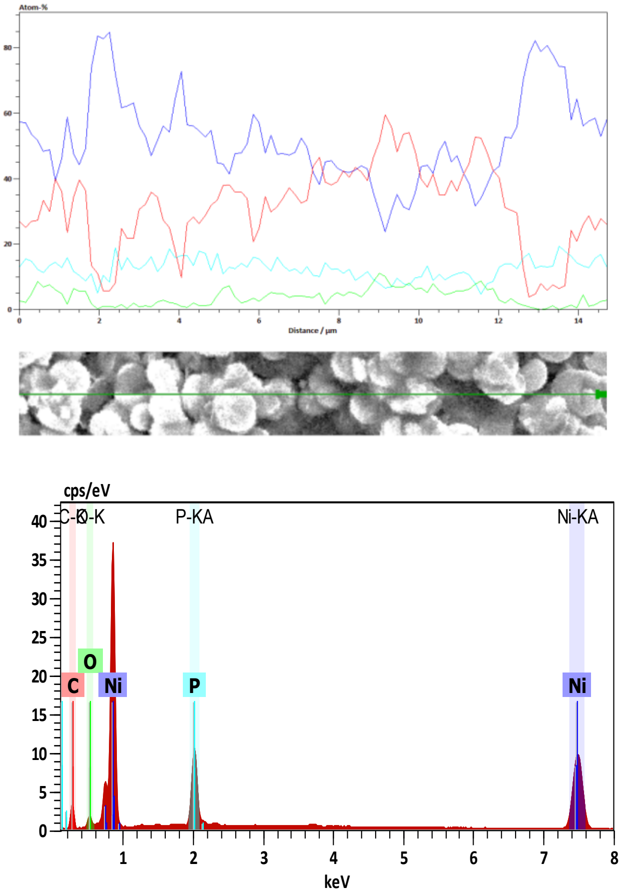

Figure 4-10 EDS elemental linescae analysis of the electroless Ni-P-GO composite coating.

Figure 4-11 reveals the polarization curves of the L80, Ni-P coating, and Ni-P-GO composite coating. As demonstrated, the corrosion potentials were shifted to more noble values by applying the Ni-P and Ni-P-GO composite coatings. Moreover, the corrosion potential of the Ni-P-GO composite coating is much less negative than Ni-P coating. The corrosion current is declined by adding the graphene oxide sheets to the Ni-P coatings. Indeed, the presence of the graphene oxide sheets considerably declined the corrosion current of the electroless Ni-P coatings.

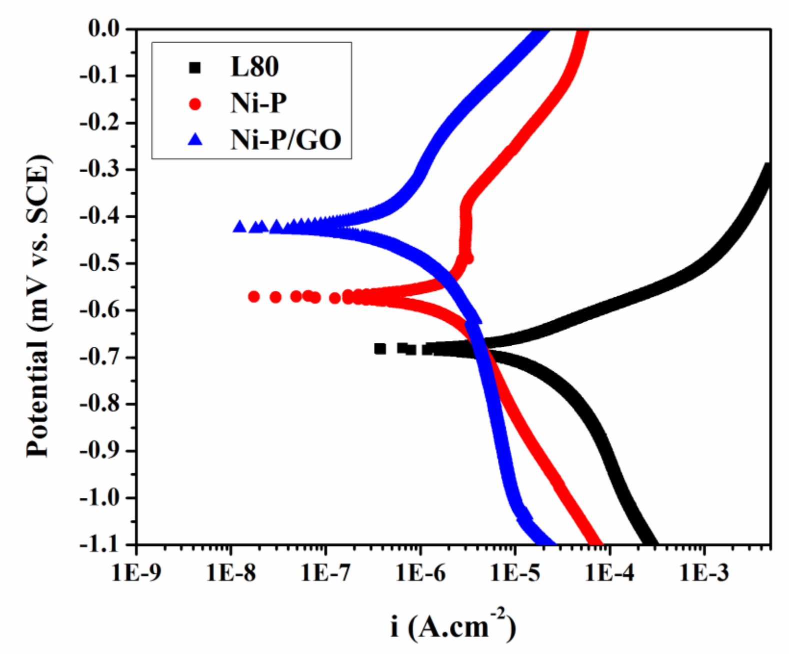

Figure 4-11 Polarization test results of the L80, Ni-P coating, and Ni-P-GO composite coating.

GO nanosheets in composite coating can create a tortuous path and also fill up the very small pores existing in the coating which results in decreasing the transmission of corrosive ions to the substrate [70]. By adding graphene oxide nanosheets grain size is decreased and the corrosion path is significantly distorted due to the incorporations of GO nanosheets in the Ni-P matrix [71]. GO sheet itself provides an extra barrier to block the corrosive ions diffusion into the matrix, which then protects the underlying metals from corrosion attack [71].

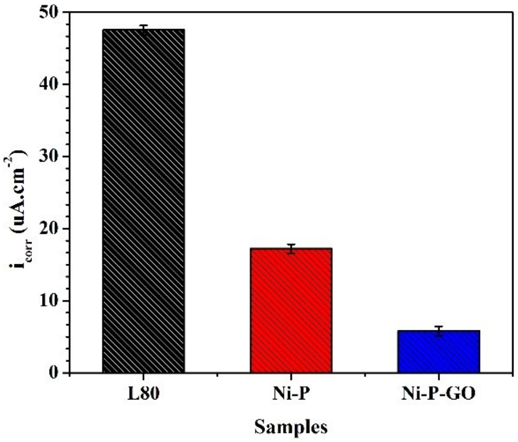

Figure 4-12 Corrosion current of L80 steel, Ni-P, and Ni-P-GO composite coatings.

Corrosion current of the L80, Ni-P coating, and Ni-P-GO composite coating is demonstrated in Figure 4-12. Graphene oxide is chemically very stable [34], and when we add GO to Ni-P coating, the effective metallic area at the coating-corrosive environment is decreased. So, by adding GO, we increase the chemical stability of the Ni-P coating. Due to the fact that the honeycomb hexagonal lattice of GO is disrupted by some functional groups (hydroxyl (OH), carboxyl (COOH) and epoxide (-O-)), GO is an electrical insulator [35]. The GO nanosheets distributed uniformly in the Ni-P coating can interrupt the flow of current between anodic and cathodic areas of the matrix. Figure 4-13 demonstrates FESEM images taken from the surface of Ni-P coating (a and b) and Ni-P-GO composite coating (b and d) after conducting the polarization tests in the sour environment.

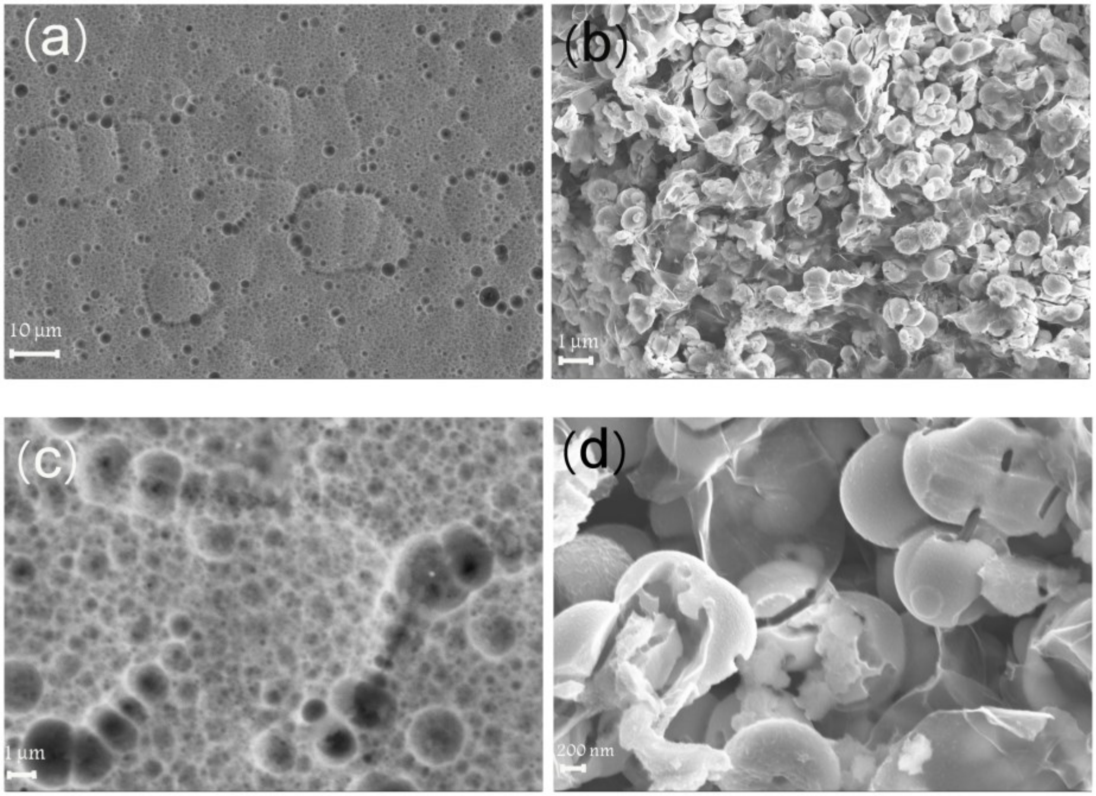

Figure 4-13 FESEM images taken from the surface of Ni-P coating (a and c) and Ni-P-GO composite coating (b and d) after the corrosion test.

As shown in Figure 4-13, the Ni-P coating was severely affected by localized corrosion, while the presence of GO in Ni-P-GO composite coating considerably decreased the intensity of the localized corrosion, and also it can be mentioned that by adding graphene oxide there is a shift from localized corrosion to the uniform corrosion. At the same magnification (Figure 4-13 (b) and (c)), the pits formed on the surface of the Ni-P-GO composite coating cannot be readily recognized since it was corroded almost uniformly; however, the localized corrosion of the Ni-P coating is clearly observed.

As schematically demonstrated in Figure 4-14, due to the presence of GO nanosheets functioning as barriers against the corrosion ions, and less available paths for corrosion proceeding, Ni-P-GO composite coating represented a much higher corrosion resistance in comparison with that of the Ni-P coating. In fact, adding the GO nanosheets forms a net structure in the coating matrix (as demonstrated in Figure 4-14) which can considerably prevent the corrosive ions from being diffused through the coating.

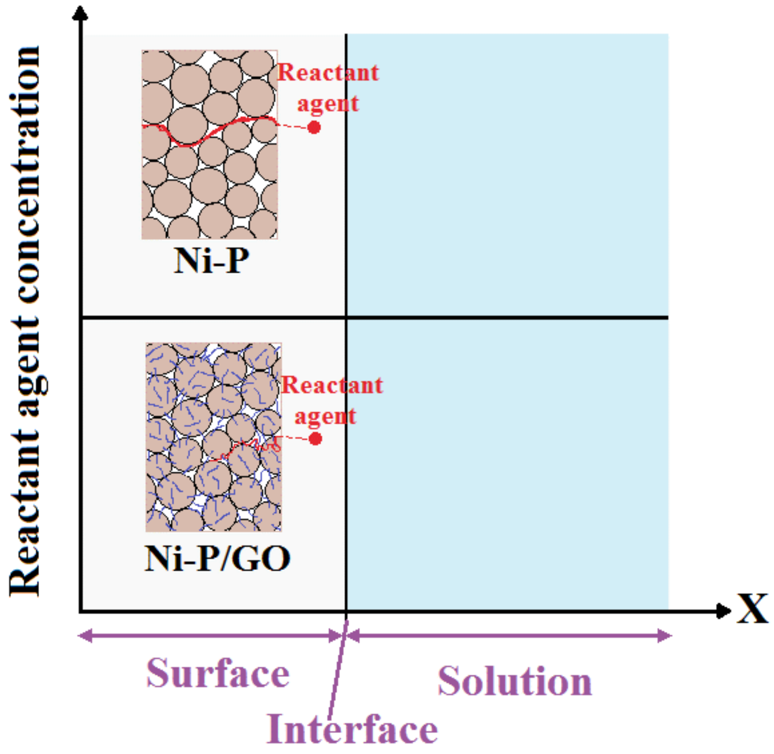

Figure 4-14 Schematic view of the structure of the Ni-P coating and Ni-P-GO composite coating from cross section during the corrosion process.

GO nanosheets (as the additive particle to the coating) can fill up the very small pores existing in the Ni-P coating [9], making the coating more compact and improving the electrochemical stability of the coating in a corrosive environment. The presence of GO nanosheets in the Ni-P coating functions as an obstacle against the diffusion of the corrosive ions, which can further diminish the chemical reactions between the corrosive environment and the coating. Microstructure of the coating has a considerable effect on the diffusion of the corrosive ions to the matrix, and the electrochemical reactions at the interface of the coating and corrosive environment. Figure 4-15 illustrates the Nyquist plot of the Ni-P coating and Ni-P-GO composite coating. Nyquist plots of all three specimens illustrate a single semi-ellipse shape.

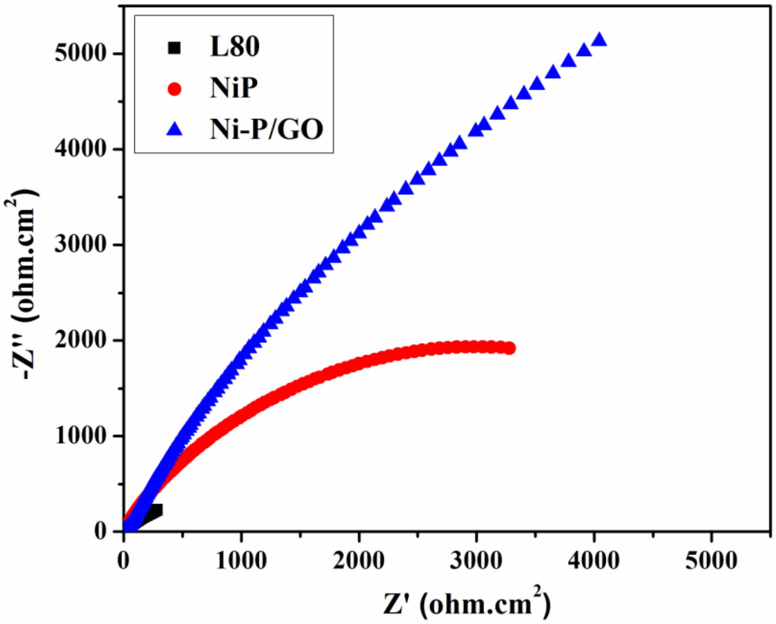

Figure 4-15 Nyquist plots of L80 carbon steel, Ni-P coating, and Ni-P-GO composite coating.

The axial radius of the EIS spectrum is associated with the total resistance. As seen, Ni-P-GO composite coating has a much higher corrosion resistance in comparison with the Ni-P coating. Figure 4-16 shows the equivalent electrical circuits of the L80 (a), and Ni-P coating and Ni-P-GO composite coating (b).

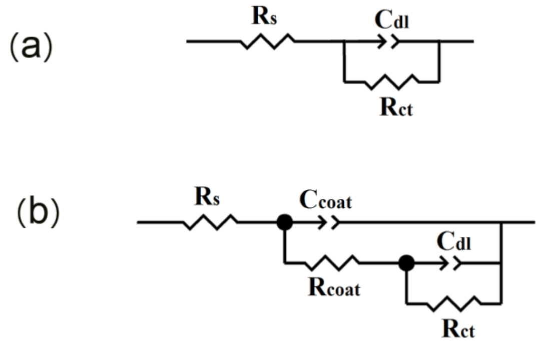

Figure 4-16 Equivalent electrical circuits of L80 (a), and Ni-P coating and Ni-P-GO composite coating (b).

The equivalent circuits consist of the charge transfer resistance (R_{ct}), electric double layer capacitance (C_{dl}), coating resistance (R_{coat}), capacitance of the coating (C_{coat}), and the solution resistance (R_s). Total resistance of the coated specimens is the sum of the R_{coat} (coating resistance against the anodic dissolution of the coating) and R_{ct} (resistance against the charge transfer reaction at the coating-solution interface). The values of R_{ct} and R_{coat} calculated according to the equivalent circuit are represented in Figure 4-16.

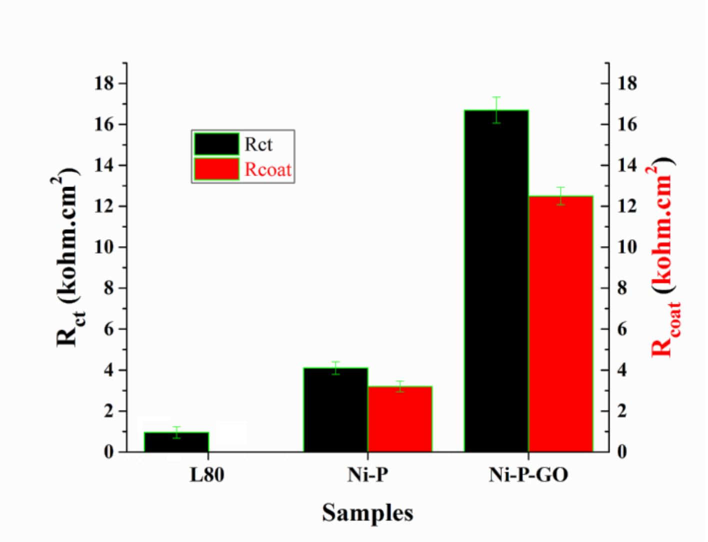

Figure 4-17 The Values of R_{coat} and R_{ct} extracted from the EIS tests.

As can be seen in Figure 4-17, the value of charge transfer resistance of carbon steel increased from 1 KΩ.cm^2 to 4 KΩ.cm^2 after applying the Ni-P coating. While value of double-layer resistance of the Ni-P coating improved up to 16 KΩ.cm^2 after adding graphene oxide to the coating. Also, the coating resistance of Ni-P coating increased from 3 KΩ.cm^2 to 12.3 KΩ.cm^2 after adding graphene oxide to the coating, representing the significant influence of GO on improving the corrosion resistance of electroless Ni-P coating.

4.4. Conclusion

In this work, Ni-P-GO composite coating was coated on L80 steel by using the electroless technique. FESEM images from the surface of the composite coatings confirmed the uniform distribution of graphene oxide. Also, FESEM images from the surface of the specimens revealed that the grain size of Ni-P-GO composite coating was smaller than that of Ni-P coating.

Electrochemical evaluations showed that adding graphene oxide to the coating significantly improved the corrosion resistance of electroless Ni-P coating in the sour environment. In addition, electrochemical impedance evaluation revealed that adding GO sheet improved the coating resistance of Ni-P coating from 1 KΩ.cm^2 to around 12.3 KΩ.cm^2.

Chapter 5: Improving the Corrosion Resistance of OCTG Carbon Steel by Gas Nitriding

5.1. Introduction

L80 carbon steel is of a great deal of interest in oil sands industry due to its desired strength and flexibility, and low cost [11, 72, 73]. Although, the corrosion of this widely used steel in corrosive environments, especially in sour oil environments is a great concern [74, 75]. There are variety kinds of surface coatings and modifications in order to improve the corrosion resistance of this alloy. Nitriding is considered as an important technique for improving the corrosion resistance of steels in corrosive environments [50, 76]. There are three kinds of nitriding techniques such as plasma, gas, and salt bath nitriding, among which the gas nitriding technique was chosen in the current study. In this technique, due to the nitrogen enrichment of the metal surface, the corrosion resistance is substantially improved in the corrosive environments [53]. The presence of nitrogen in the metal surface leads to formation of NH^{3+} during the corrosion process, diminishing the chemical reaction of corrosive ions such as chlorine and sulfur with metal, which increases the polarization resistance and decreases the corrosion current [77]. In the work, L80 carbon steel was treated by gas nitriding process at temperature of 850 ºC and 950 ºC. After applying the nitriding process, electrochemical tests such as potentiodynamic polarization and electrochemical impedance spectroscopy were performed in a sour environment in accordance with the NACE TM0177-96standard. After the corrosion tests, the surface of the specimens was investigated by optical microscopy and SEM.

5.2. Materials and Method

The substrate for applying the gas nitriding process was L80 carbon steel, the normal chemical composition (wt.%) is C 0.32, Mn 0.80, Ni 0.016, Cu 0.12, Si 0.25, P 0.006, S 0.028, Fe balance. Samples were cut into some plates with the dimensions of 10 × 10 × 10 mm. Prior to applying the nitriding, samples were undertaken a surface preparation process. To do so, samples were first abraded by SiC waterproof paper ranging from very coarse 200 grit to very fine 2500 grit. Later on, samples were degreased in an ultrasonic bath consisting of ethanol for 15 min. Gas nitriding process was performed at the temperature of 850 ºC and 950 ºC in a nitrogen gas atmosphere with the purity of 99.9999 %, under the pressure of 2.5 bar for 2 hours. Figure 5-1 demonstrates the schematic view of the gas nitriding setup.

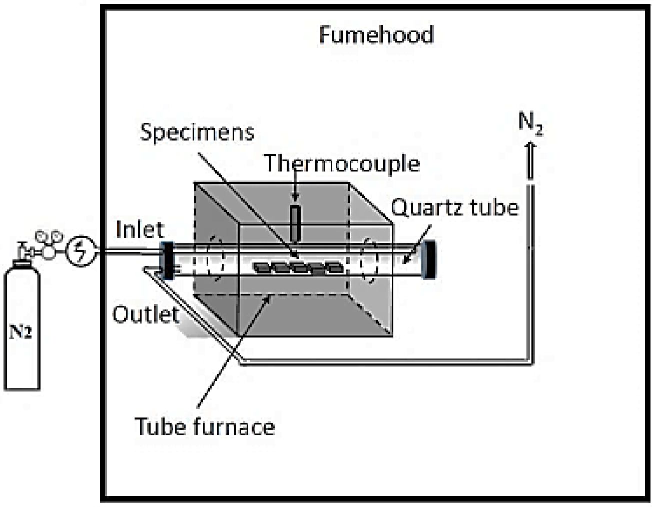

Figure 5-1 Schematic view of the gas nitriding setup.

After the nitriding process, samples were quenched in water. The corrosion test solution consisted of 5.0 wt% NaCl and 0.2 wt% acetic acid dissolved in deionized water with the pH of ~ 4. The test solution was deaerated by purging an inert gas at a rate of at least 100 mL/min for at least 1 h/L of solution. Then, the test solution was saturated with H_2S and CO_2 by purging these two gases at a rate of at least 100 mL/min for at least 20 min/L of test solution.

Electrochemical tests were performed in a three-electrode cell, where the nitrided and bare L80 steel were the working electrode, the platinum electrode was the counter electrode, and the saturated calomel electrode (SCE) was the reference electrode. Potentiodynamic polarization and EIS corrosion tests were performed by using a Gamry system potentiostat/frequency response analyzer (model 1260A) in a conventional three-electrode cell including a platinum counter electrode, a saturated calomel electrode (SCE), and reference electrode. Prior to measurement, samples were exposed to the sour environment at the open circuit potential (OCP) for 1 h. Polarization tests were performed with a scanning rate of 1 mV/s. Electrochemical parameters such as polarization resistance (R_p) and corrosion current density (i_{corr}) were calculated by interpolation of the polarization curves. EIS test was performed at the OCP over the frequency ranging from 100 KHz to 10 mHz with the potential amplitude of 10 mV. After the corrosion tests, surface morphology of the samples was investigated by optical stereoscopic microscope (OSM) (KEYENCE VHX2000), and ZEISS EVO-MA15 SEM equipped with an EDS.

5.3. Results

Figure 5-2 demonstrates the OCP variations of L80 steel and nirtided L80 steel at temperature of 850 ºC (N850) and 950 ºC (N950) in the sour environment.

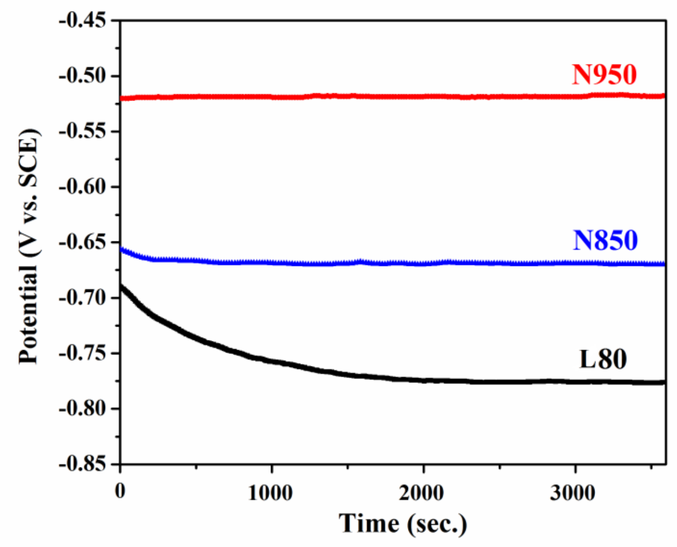

Figure 5-2 The OCP variations of L80 steel and nitrided L80 steel in the sour environment.

As can be seen, OCP of L80 sample shifted gradually to negative potential; however, the OCPs of the nitride specimens remained relatively constant over the time. The sample modified by nitriding process revealed more noble potential value, specifically the specimen nitrided at the temperature of 950 ºC. The potentiodynamic polarization curves of the L80, N850, and N950 samples in the sour environment are illustrated in Figure 5-3.

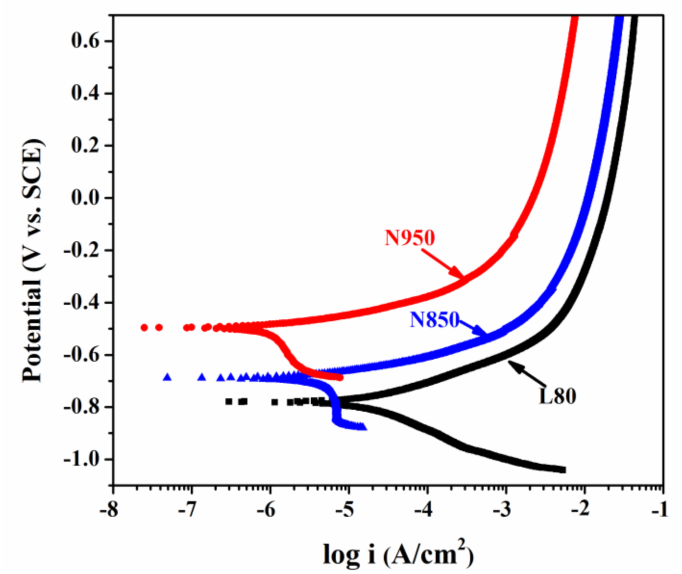

Figure 5-3 Potentiodynamic polarization curves of the L80, N850, and N950 samples in the sour environment.

The value of some electrochemical parameters such as polarization resistance (R_p) and corrosion current density (i_{corr}) obtained by extrapolating the polarization curves are illustrated in Figure 5-4.

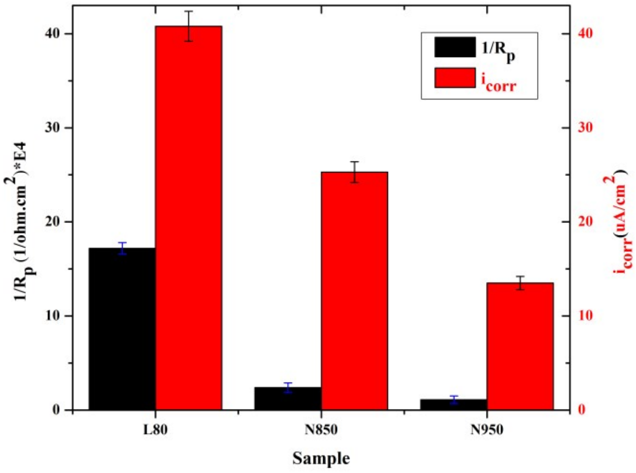

Figure 5-4 R_p and i_{corr} of the L80 and the nitrided samples.

As shown in Figure 5-4, by applying the gas nitriding as a surface modification technique, the corrosion current and polarization resistance of L80 steel significantly decreased and increased, respectively. Figure 5-5 depicts the optical microscope images taken from the surface of the L80, N850, and N950 samples after the polarization test. The surface corrosion and formation of corrosion products can be clearly seen on the surface of samples in Figure 5-5. Indeed, degradation and subsequently the presence of corrosion products on the surface of N850 specimen is less than that of the L80 specimen. In addition, surface degradation of the N950 specimen caused by the corrosion reactions is much lower than that of N850 sample.

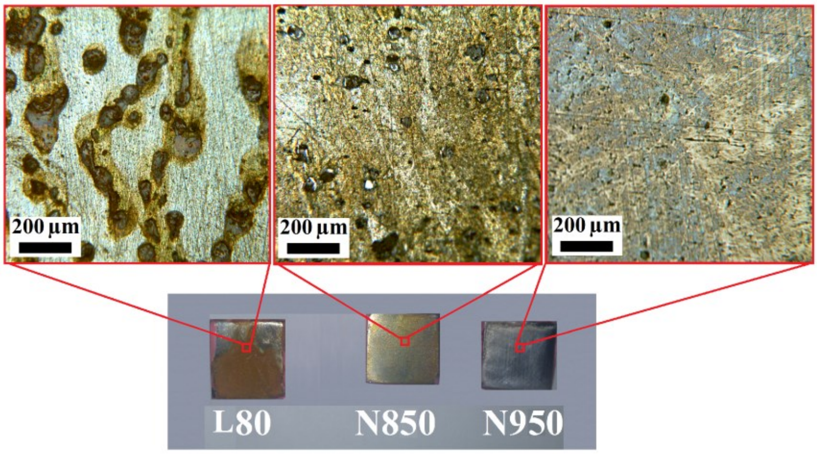

Figure 5-5 The optical microscope images from the surface of L80, N850, and N950 samples after the polarization test.

In addition, the intensity of localized corrosion on the surface of L80 sample is higher than that of N850 and N950 specimens. By applying the gas nitriding process, the size of pits declined considerably, and localized corrosion distribution became more uniform. In other words, localized corrosion intensity of the modified samples (specifically N950) decreased significantly in comparison with the L80 sample. Nyquist and Bode plots of the L80, N850, and N950 samples are demonstrated in Figure 5-6 and Figure 5-7, respectively.

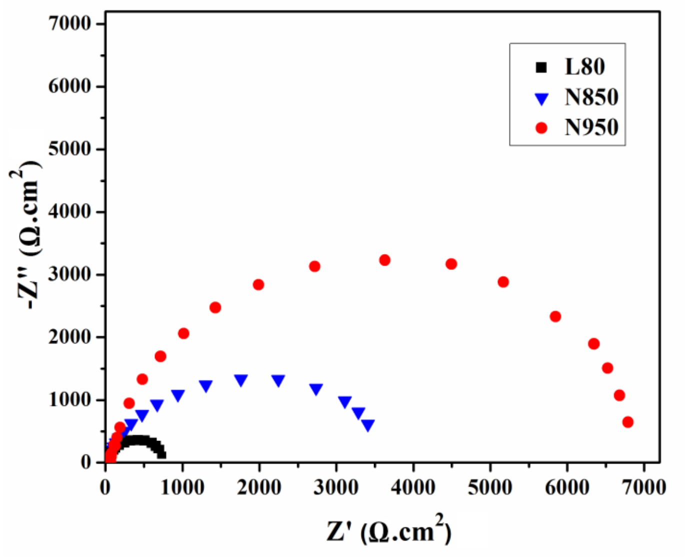

Figure 5-6 Nyquist plots of the L80, N850, and N950 samples.

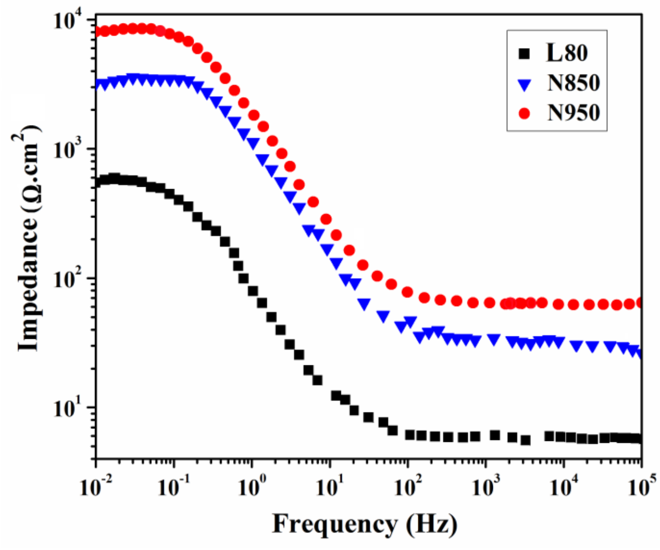

Figure 5-7 Bode plots of the L80, N850, and N950 samples.

The minimum and maximum curve radius of the Nyquist plots belongs to the L80 and N950 specimens. The higher the curve radius, the greater the corrosion resistance. Also, as shown in Bode plots, the corrosion resistance of the specimens modified by gas nitriding improved desirably. Figure 5-8 demonstrates the equivalent electrical circuits of the samples

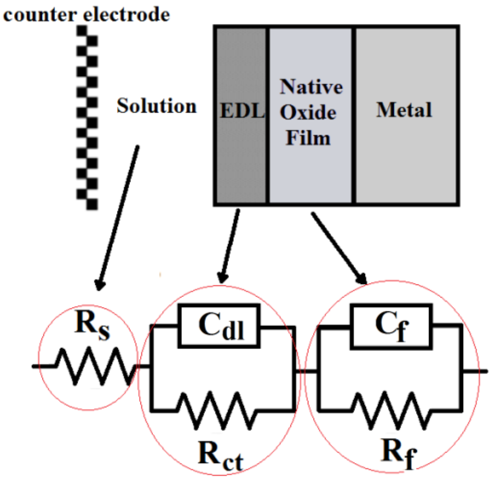

Figure 5-8 The electrical equivalent circuit of the samples.

The represented equivalent circuit is consisting of oxide film resistance (R_f), electrical capacity of oxide film (C_f), charge transfer resistance (R_{ct}), electrical capacity of double layer (C_{dl}), and solution resistance (R_s). The corrosion resistance of specimens is determined by measuring the value of R_{ct} (resistance against the charge transfer reaction at the coating-solution interface) and R_f (the resistance against the diffusion of corrosive ions though the oxide film resulting in anodic dissolution of the metal) [78]. The value R_f and R_{ct} for both L80 and the ones modified by gas nitriding is represented in Figure 5-9.

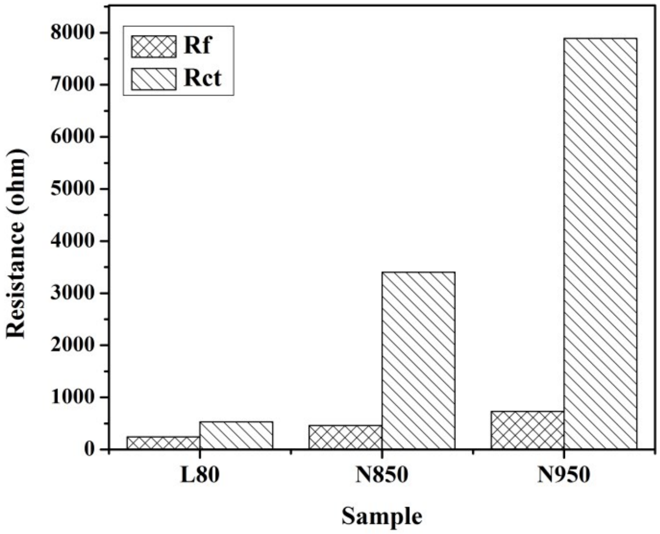

Figure 5-9 The values of Rf and Rct L80, N850, and N950 samples.

As shown in Figure 5-9, the value of R_{ct} and R_f for the specimen modified by gas nitriding at 950 ºC (N950) is much higher than that of the L80 specimen. Charge transfer resistance is considered as the major parameter for evaluating the corrosion behavior, indicating the ions reaction in corrosive environment with the surface of the oxide layer. By increasing the value of R_{ct}, the surface resistance of specimen against the corrosive ions diffused to the oxide layer is increased.

5.4. Discussion

Beyond 700 °C, molecular nitrogen is converted to atomic nitrogen, and the converting rate becomes stable above 950 °C. In fact, atomic nitrogen can diffuse into the carbon steel easier than the molecular nitrogen [79]. So, that is why, 850 °C and 980 °C was selected in this study.

Many studies [77-79] reported that, increasing the amount of nitrogen in steels can substantially improve their localized corrosion resistance. Some mechanisms were proposed in order to interpret the impact of nitrogen on improving the corrosion resistance of steels, which is presenting as following.

5.4.1. Formation of Ammonium at the Metal-Corrosive Environment Interface

Nitrogen on the steel surface is converted to the ammonium ions (according to the Reaction (5-1) when it is exposed to the corrosive environment [81].

$$[N] + 4H^+ + 3e^- \longrightarrow NH_4^+ \qquad (5\text{-}1)$$

Baba and his colleagues [82] reported the presence of NH_3 and NH_4^+ by doing XPS analysis on the nitrided steel after the corrosion test. Baba proposed that, the formation of ammonium at the interface of steel and corrosive environment consumes the protons and prevents the pH from being decreased at the initial pits [79, 80]. In addition, NH_4^+ ions decline the probability of the corrosive ions reactions with the substrate metal, providing an appropriate condition for reforming the passive layer. The quick formation of the passive film after even appearing a crack on it can significantly suppress the localized corrosion. Furthermore, it shifts the surface corrosion behavior from the localized corrosion to a uniform corrosion. As a result, the presence of nitrogen improves the pitting corrosion resistance of steel through reforming or repairing the passive film. According to some studies, the formation rate of NH_4^+ enhances by increasing the amount of nitrogen in steel [79, 80]. Baba et al. reported that, the required amount of H^+ to form NH_4^+ in the pits is proportional to the amount of nitrogen in steel [79, 80].

5.4.2. Formation of Nitrate

The deterrent effect of nitrates against the pitting corrosion was approved by some researchers [83, 84]. Misawa [84] had conducted some theoretical studies on this regard and proposed that, formation of nitrate through the dissolution process can considerably prevent the growth of pits; moreover, it can function as a deterrent agent against the pitting corrosion at the elevated potentials. NH_4^+ can form some deterrent agents such as NO_2^- and NO_3^- according to the Reaction (5-2).

$$NH_4^+ + 2H_2O \longrightarrow NO_2^- + 8H^+ + 6e^- \qquad (5\text{-}2)$$

Although, formation of ammonium ions according to the Reaction (5-2) may be considered as a more plausible mechanism for indicating the deterrent effect of nitrate [82-84].

$$NO_3^- + 10H^+ + 8e^- \longrightarrow 3H_2O + NH_4^+ \qquad (5\text{-}3)$$

In accord with the polarization and electrochemical impedance curves, decreasing the corrosion current density, and increasing the charge transfer resistance of the nitrided L80 samples in comparison with the L80 sample is primarily due to the presence of nitrogen ions on the metal surface and formation of a dense layer which stabilized by nitrogen. The initiation of localized corrosion for the nitrided specimens is postponed; furthermore, the pits growth is substantially confined due to the prompt repassivation process, resulting in decreasing the pitting corrosion substantially [80, 82, 83]. Surface morphology and EDS elemental mapping analysis of L80 and N950 samples after the corrosion test are depicted in Figure 5-10. As demonstrated, the presence of some elements such as sulfur, oxygen, and chlorine in N950 specimen decreased considerably in comparison with L80 specimen.

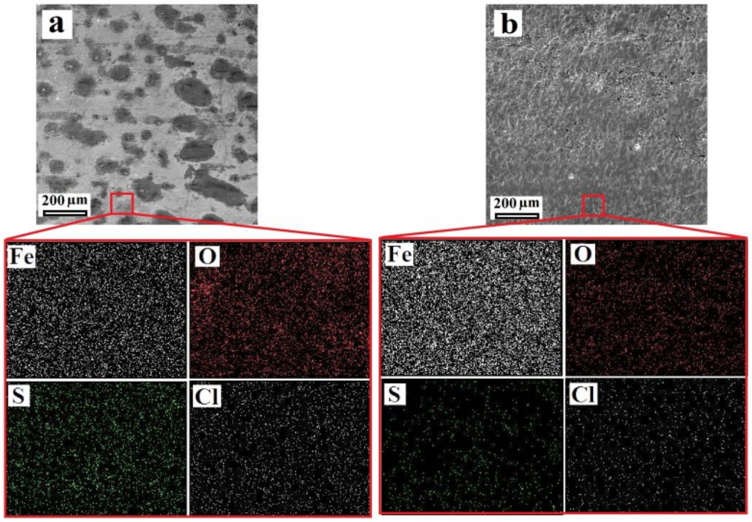

Figure 5-10 Surface morphology and EDX elemental mapping analysis of L80 (a) and N950 (b) samples after the corrosion tests.

5.4.3. Presence of a Nitrogen-Rich Layer in the Surface Layer of the Metal Oxide

Formation of a nitrogen-rich layer in the surface layer of the nitrided steel was confirmed and reported [87]. The presence of nitrogen in the oxide passive layer leads to formation of a dense and protective oxynitride layer. This nitrogen-rich layer stabilizes and improves the corrosion resistance of the metal surface against the corrosive ions [87].

5.5. Conclusions

Gas nitriding process was applied on L80 OCTG steel at the temperature of 850 ºC and 950 ºC. The results of the potentiodynamic polarization and EIS tests in sour environment revealed a considerable increase in corrosion resistance of the nitrided L80 steel. According to the results obtained from the electrochemical tests, by applying the gas nitriding process at 950 ºC, the corrosion resistance of the L80 specimen in the sour environment increased from 569 $\Omega.cm^2$ to 7748 $\Omega.cm^2$. Moreover, the microscopic images taken from the samples surface after the polarization test revealed that the surface degradation of the nitrided L80 steel decreased desirably in comparison with the L80 steel. In other words, the localized corrosion resistance of the modified samples specifically the sample nitrided at 950 ºC improved substantially.

Chapter 6: Conclusions

- ✓ Electroless Ni-P coating and coated (EN coating) and uncoated carbon steel used in SAGD operation for some months was evaluated by OSM, FESEM, EDS, and XRD. Results revealed that the electroless Ni-P coating significantly improved the corrosion resistance of the slotted liner made of carbon steel. EDS elemental mapping analysis from the cross section and XRD results from the surface of the scales showed the formation of a condensed layer of nickel sulfide including NiS and Ni_3S_2 on the top layer of the scale which can function as a barrier against the corrosive sour environment. Also, XRD results showed the presence of a stable intermetallic phases (such as Ni_3P) in the OCTG steel coated by EN coating. The scale formed on the uncoated OCTG steel was so porous in comparison with the scale formed on the EN coated OCTG steel. Sulfur was observed through the porous scale of the uncoated slotted liner. Actually, sulfur diffused though the scale formed on the uncoated carbon steel.

- ✓ A novel coating - Ni-P-GO composite coating - was coated on L80 carbon steel by using the electroless technique. FESEM images from the surface of the composite coating confirmed the uniform distribution of the graphene oxide. Also, surface microscopic images showed that, the grain size of the Ni-P-GO composite coating was smaller than that of Ni-P coating. Electrochemical evaluations revealed that adding the single layer graphene oxide nano-sheets improved the corrosion resistance of the electroless Ni-P coating in the sour environment. Electrochemical impedance evaluation showed that, adding GO improved the coating resistance of Ni-P coating from 1 $K\Omega.cm^2$ to around 12.3 $K\Omega.cm^2$.

✓ Gas nitriding (at different temperature of 850 ºC and 950 ºC) was employed in order to improve the corrosion resistance of the L80 steel. The results of the potentiodynamic polarization and EIS tests in sour environment revealed a considerable increase in corrosion resistance of the nitrided L80 steel. The electrochemical test results revealed that, by applying the gas nitriding process at 950 ºC, the corrosion current density of the L80 sample in the sour environment the corrosion resistance enhanced from 569 $\Omega.cm^2$ to 7748 $\Omega.cm^2$. Microscopic images taken from the samples surface after the corrosion tests revealed that the surface degradation of the nitrided L80 steel decreased desirably in comparison with the L80 steel. Indeed, the localized corrosion resistance of the modified samples specifically the sample nitrided at 950 ºC improved substantially.

Chapter 7: Further Work

7.1. Long Term Stability of the Coating Solution

The concentration of lead ion in the coating solution will be optimized to achieve a coating solution which will be stable for a long time after adding GO nanosheets. A very low amount of heavy metal ion stabilizers is good enough to accomplish the function. Indeed, stabilizers decline the activity of the electroless coating solution. X. Yin et al. reported that, Pb^{2+} can be as a good stabilizer for Ni-P coating [88].

7.2. Erosion Corrosion of Ni-P-GO Composite Coating

Ni-P-GO composite coating is a new coating and just a few works have been done on this kind of composite coating [65, 86]. Mostly they focused on evaluating the corrosion resistance. However, the erosion resistance of this coating have not studied yet. Erosion of the SAGD slotted liners is a mechanical wear process, resulting in the mass loss of the material by a slurry including sand and fluid flow. Basically, the combined impact of erosion and corrosion are considerably higher than the sum of the effects of individual processes [85]. B.T. Lu et al. evaluated the anodic current densities of 304 stainless steel and carbon steels in flowing slurries under potentiostatic control condition and they determined the kinetic parameters of repassivation [90]. In addition, Lu reported that, slurry impingement may facilitate the pit formation [91].

The erosion-corrosion of the coated (Ni-P-GO composite coating) and uncoated (carbon steel) specimens can be investigated by a jet-impingement facility. The range of the sand concentration can be between 0 and 2 wt% (which is close to the SAGD operation). A Gamry instrument potentiostat might be utilized to firstly provide in situ information on the current/voltage response of the specimens in the special experimental conditions, and second it can provide the opportunity to control the chemical reactions occurring on the specimen's surface. Schematic view of the proposed erosion-corrosion setup is shown in Figure 7-1.

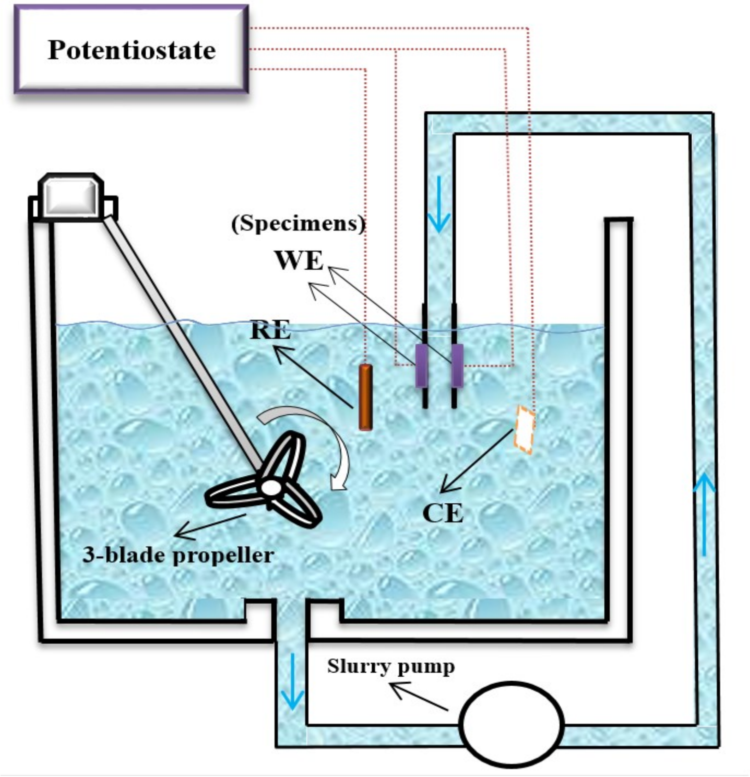

Figure 7-1 Schematic view of the erosion-corrosion setup.

7.3. Elevated-Temperature Corrosion Tests

In order to get closer to the real situation of the SAGD operation, it would be good idea to investigate the corrosion resistance at the elevated temperature in the simulated sour environment.

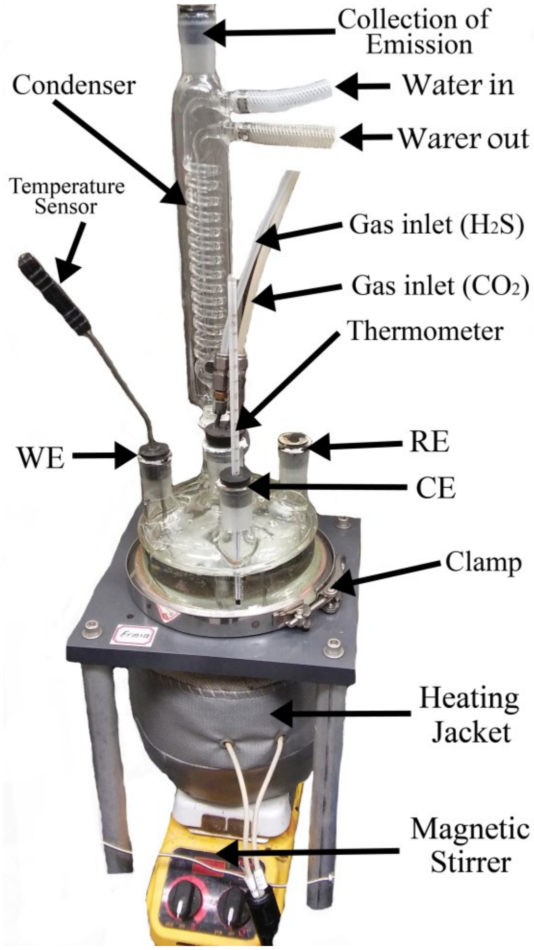

Figure 7-2 Corrosion setup for the elevated temperature tests.

I have prepared a setup for evaluating the corrosion behavior of the carbon pipeline steel, Ni-P coating, and Ni-P-GO composite coatings in the simulated environment saturated by H_2S and

CO_2, in order to evaluate the effect of temperature on corrosion properties. The elevated-temperature corrosion test setup that I have prepared is demonstrated in Figure 7-2. Temperature can be increased up to 98 °C. Moreover, I have calibrated the heating system and the results are tabulated in Table 7-1.

Table 7-1 Calibration of the heating system.

	Controller temperature	Sensor temperature	Thermometer
Stage 1	25 ºC	37 ºC	40 ºC
Stage 2	40 ºC	41 ºC	44 ºC
Stage 3	45 ºC	51 ºC	53 ºC
Stage 4	55 ºC	57 ºC	61 ºC
Stage 5	65 ºC	70 ºC	74 ºC
Stage 6	75 ºC	81 ºC	85 ºC
Stage 7	85 ºC	88 ºC	93 C

References

[1] T. Q. C. Dang, Z. Chen, T. B. N. Nguyen, W. Bae, and C. L. Mai, “Numerical simulation of SAGD recovery process in presence of shale barriers, thief zones, and fracture system,” *Pet. Sci. Technol.*, vol. 31, no. 14, 2013.

[2] L. C. R. M. Butler, “Numerical Simulation of the Steam-assisted Gravity Drainage Process (SAGD),” *J. Can. Pet. Technol.*

[3] J. A. Mclennan and C. V Deutsch, “SAGD Reservoir Characterization Using Geostatistics : Application to the Athabasca Oil Sands , Alberta , Canada,” pp. 1–21.

[4] J. Jimenez and S. I. Exploration, “The Field Performance of SAGD Projects in Canada,” in *International Petroleum Technology Conference*, 2008.

[5] Z. B. Z. Ahmedzhanov T.K., Nuranbaeva B.M. and B. B. B. Julomanov T.D., “DEVELOPMENT INNOVATIVE METHODS FOR INCREASING OIL RECOVERY DURING THE PRODUCTION OF HIGH-VISCOSITY AND PARAFFIN OIL,” *Kazakh National Technical University*.

[6] J. W. Jang, P. G. Kim, K. N. Tu, D. R. Frear, and P. Thompson, “Solder reaction-assisted crystallization of electroless Ni–P under bump metallization in low cost flip chip technology,” *J. Appl. Phys.*, vol. 85, no. 12, p. 8456, 1999.

[7] B. D. Craig and L. Smith, “Corrosion Resistant Alloys (CRAs) in the oil and gas industry - selection guidelines update,” *Nickel Inst. Tech. Ser.*, pp. 10073, 2011.

[8] R. Parkinson, “Properties and Applications of Electroless Nickel,” *Nickel Dev. Inst. Publ.*, p. 33, 1997.

[9] H. Luo, M. Leitch, Y. Behnamian, Y. Ma, H. Zeng, and J. Luo, “Development of electroless Ni–P/nano-WC composite coatings and investigation on its properties,” *Surf. Coat. Technol.*, vol. 277, pp. 99–106, 2015.

[10] M. Koteeswaran, “CO_2 and H_2S Corrosion in Oil Pipelines,” pp. 1-79, 2010.

[11] J. M. Gray and F. Siciliano, “High Strength Microalloyed Linepipe : Half a Century of

Evolution," *Proc. an Int. Symp. high-strength, low-alloy steels.*, pp. 1-26, 1959.

[12] L. M. Abrantes and J. P. Correia, "P Plating-On the Mechanism of Electroless Ni service Email alerting On the Mechanism of Electroless Ni-P Plating," *J. Electrochem. Soc*, vol. 141, pp. 2356-2360, 1994.

[13] M. Schlesinger and M. Paunovic, "Frontmatter," *Mod. Electroplat. 5th Ed.*, pp. 309–326, 2010.

[14] P. Sahoo and S. K. Das, "Tribology of electroless nickel coatings - A review," *Mater. Des.*, vol. 32, pp. 1760–1775, 2011.

[15] R. C. Agarwala and V. Agarwala, "Electroless alloy/composite coatings : A review," *Sadhana*, vol. 28, no. August, pp. 475-493, 2003.

[16] J. Sudagar, J. Lian, and W. Sha, "Electroless nickel, alloy, composite and nano coatings - A critical review," *J. Alloys Compd.*, vol. 571, pp. 183-204, 2013.

[17] H. Xu, Z. Yang, M. K. Li, Y. L. Shi, Y. Huang, and H. L. Li, "Synthesis and properties of electroless Ni-P-Nanometer Diamond composite coatings," *Surf. Coatings Technol.*, vol. 191, pp. 161-165, 2005.

[18] K. H. Hur, J. H. Jeong, and D. N. Lee, "Microstructures and crystallization of electroless Ni-P deposits," *J. Mater. Sci.*, vol. 25, pp. 2573-2584, 1990.

[19] F. B. Mainier, M. P. C. Fonseca, S. S. M. Tavares, and J. M. Pardal, "Quality of electroless Ni-P (nickel-phosphorus) coatings applied in oil production equipment with salinity," *J. Mater. Sci. Chem. Eng.*, vol. 1, pp. 1-8, 2013.

[20] S. Kundu, S. K. Das, and P. Sahoo, "Properties of electroless Nickel at elevated temperature - A review," *Procedia Eng.*, vol. 97, pp. 1698-1706, 2014.

[21] M. Ebrahimian-Hosseinabadi, K. Azari-Dorcheh, and S. M. M. Vaghefi, "Wear behavior of electroless Ni-P-B4C composite coatings," *Wear*, vol. 260, pp. 123-127, 2006.

[22] J. B. H. G.O. Mallory, "Electroless plating: Fundamentals and Applications," *Am. Electroplat. Surf. Finischers Soc.*, p. 539, 1990.

[23] M. Momenzadeh and S. Sanjabi, "The effect of TiO_2 nanoparticle codeposition on

microstructure and corrosion resistance of electroless Ni-P coating," *Mater. Corros.*, vol. 63, pp. 614-619, 2012.

[24] S. R. Allahkaram, R. F. Alivand, and M. S. Bakhsh, "CORROSION BEHAVIOR OF ELECTROLESS Ni-P / NANOZnO COATINGS," vol. 10, 2013.

[25] J. Colaruotolo and D. Tramontana, "Engineering Applications of Electroless Nickel," *Electroless Plat.*, pp. 207-226, 1990.

[26] J. N. Balaraju and K. S. Rajam, "Electroless deposition and characterization of high phosphorus," *Int. J. Electrochem. Sci.*, vol. 2, pp. 747–761, 2007.

[27] Y. S. Huang, X. T. Zeng, X. F. Hu, and F. M. Liu, "Corrosion resistance properties of electroless nickel composite coatings," *Electrochim. Acta*, vol. 49, pp. 4313–4319, 2004.

[28] N. Feldstein, "Chapter 11: Composite Electroless Plating," *Electroless Plat. Fundam. Appl.*, pp. 269-287.

[29] M. Firoozbakht, S. M. Monirvaghefi, and B. Niroumand, "Electroless composite coating of Ni-P-carbon nanotubes on magnesium powder," *J. Alloys Compd.*, vol. 509, pp. 496-502, 2011.

[30] M. Alishahi, S. M. Monirvaghefi, A. Saatchi, and S. M. Hosseini, "The effect of carbon nanotubes on the corrosion and tribological behavior of electroless Ni-P-CNT composite coating," *Appl. Surf. Sci.*, vol. 258, pp. 2439-2446, 2012.

[31] S. J. Richard Prabakar, Y. H. Hwang, E. G. Bae, D. K. Lee, and M. Pyo, "Graphene oxide as a corrosion inhibitor for the aluminum current collector in lithium ion batteries," *Carbon N. Y.*, vol. 52, pp. 128-136, 2013.

[32] Z. Gao, S. Zhao, Y. Wang, X. Wang, and L. Wen, "Corrosion behavior and wear resistance characteristics of electroless Ni-P-CNTs plating on carbon steel," *Int. J. Electrochem. Sci.*, vol. 10, pp. 637-648, 2015.

[33] D. Scientiae and M. Universitatis, *JAY MONDAL, "Novel Corrosion Protective Nanostructured Composite Coatings,"*. 2015.

[34] F. Perrozzi, S. Prezioso, and L. Ottaviano, "Graphene oxide: from fundamentals to

applications," *J. Phys. Condens. Matter*, vol. 27, p. 13002, 2015.

[35] V. V. Chaban and O. V. Prezhdo, "Structure and energetics of graphene oxide isomers: ab initio thermodynamic analysis," *Nanoscale*, vol. 7, pp. 17055-17062, 2015.

[36] E. Jimenez, C. Amieva, J. L. Barroso, A. Laura, M. Hernández, and C. V. Santos, "Graphene-Based Materials Functionalization with Natural Polymeric Biomolecule*s,*". *Edgar Jimenez-Cervantes Amieva*, 2016.

[37] J. N. Balaraju, T. S. N. Sankara Narayanan, and S. K. Seshadri, "Electroless Ni-P composite coatings," *J. Appl. Electrochem.*, vol. 33, pp. 807-816, 2003.

[38] G. H. Street, "D E P O S I T I O N OF COMPOSITE AUTOCATALYTIC NICKEL 1 . I n t r o d u c t i o n," vol. 13, pp. 119-125, 1981.

[39] A. Baghizadeh, D. A. A. Gol, O. R. Kakuee, A. R. T. Taher, M. L. Rashti, and M. F. Farahani, "INFLUENCE OF PARTICLE SIZE ON CORROSION RESISTANCE OF ELECTROLESS Ni-P-SiC COMPOSITE COATINGS," *Iran. J. Sci. Technol. Trans. B Eng.*, vol. 34, pp. 1-12, 2008.

[40] J. N. Balaraju, Kalavati, and K. S. Rajam, "Influence of particle size on the microstructure, hardness and corrosion resistance of electroless Ni-P-Al2O3 composite coatings," *Surf. Coatings Technol.*, vol. 20, pp. 3933-3941, 2006.

[41] X. Shu, Y. Wang, C. Liu, A. Aljaafari, and W. Gao, "Double-layered Ni-P/Ni-P-ZrO2 electroless coatings on AZ31 magnesium alloy with improved corrosion resistance," *Surf. Coatings Technol.*, vol. 261, pp. 161-166, 2015.

[42] S. R. Ardakani, A. Afshar, S. Sadreddini, and A. A. Ghanbari, "Characterization of Ni-P-SiO2-Al2O3 nano-composite coatings on aluminum substrate," *Mater. Chem. Phys.*, vol. 189, pp. 207-214, 2016.

[43] Y. Wang, J. He, W. Wang, J. Shi, N. Mitsuzaki, and Z. Chen, "Preparation and characterization of Ni-P/Ni3.1B composite alloy coatings," *Appl. Surf. Sci.*, vol. 292, pp. 462-468, 2014.

[44] H. Luo, X. Wang, S. Gao, C. Dong, and X. Li, "Synthesis of a duplex Ni-P-YSZ/Ni-P

nanocomposite coating and investigation of its performance," *Surf. Coatings Technol.*, vol. 311, pp. 70-79, 2017.

[45] C. I. Hsu, G. L. Wang, M. Der Ger, and K. H. Hou, "Corrosion behaviour of electroless deposited Ni-P/BN(h) composite coating," *Int. J. Electrochem. Sci.*, vol. 11, pp. 4352-4361, 2016.

[46] Y. Lixia, L. Ying, L. Guannan, L. Zhenghui, and W. Guixiang, "Preparation and Properties of Electroless Plating Wear- resistant and Antifriction Composite Coatings Ni-P-SiC- WS2," *Rare Met. Mater. Eng.*, vol. 44, pp. 28-31, 2015.

[47] M. H. Sadhir, M. Saranya, M. Aravind, A. Srinivasan, A. Siddharthan, and N. Rajendran, "Comparison of in situ and ex situ reduced graphene oxide reinforced electroless nickel phosphorus nanocomposite coating," *Appl. Surf. Sci.*, vol. 320, pp. 171-176, 2014.

[48] S. R. Meka, A. Chauhan, T. Steiner, E. Bischoff, P. K. Ghosh, and E. J. Mittemeijer, "Generating duplex microstructures by nitriding; nitriding of iron based Fe–Mn alloy," *Mater. Sci. Technol.*, vol. 1, p. 174, 2015.

[49] C. X. Li and T. Bell, "Corrosion properties of plasma nitrided AISI 410 martensitic stainless steel in 3.5% NaCl and 1% HCl aqueous solutions," *Corros. Sci.*, vol. 48, pp. 2036-2049, 2006.

[50] H. Hänninen, J. Romu, R. Ilola, J. Tervo, and A. Laitinen, "Effects of processing and manufacturing of high nitrogen-containing stainless steels on their mechanical, corrosion and wear properties," *J. Mater. Process. Technol.*, vol. 117, pp. 424-430, 2001.

[51] A. International, "Process Selection Guide," *Surf. Hardening Steels Underst. Basics*, pp. 1-16, 2002.

[52] A. Biswas, L. Li, U. K. Chatterjee, I. Manna, S. K. Pabi, and J. Dutta Majumdar, "Mechanical and electrochemical properties of laser surface nitrided Ti-6Al-4V," *Scr. Mater.*, vol. 59, pp. 239-242, 2008.

[53] I. Gunes, M. Erdogan, and A. Gürhan, "Corrosion behavior and characterization of plasma nitrided and borided AISI M2 steel," *Mater. Res.*, vol. 17, pp. 612-618, 2014.

[54] X. Chen, “The Study of the Corrosion Behavior of Gas Nitriding Treated L80 Steel in Simulated Environment for the Slotted Liners of SAGD,” University of Alberta, 2016.

[55] K. K. Kantola, “Modelling, Estimation and Control of Electroless Nickel Plating Process of Printed Circuit Board Manufacturing,“. 2006.

[56] Q. Y. Wang, X. Z. Wang, H. Luo, and J. L. Luo, “A study on corrosion behaviors of Ni-Cr-Mo laser coating, 316 stainless steel and X70 steel in simulated solutions with H_2S and CO_2,” *Surf. Coatings Technol.*, vol. 291, pp. 250-257, 2016.

[57] S. C. Koria, “Materials and Energy Balance in Metallurgical Processes,” *Kanpur*, 2017.

[58] I. Grozdanov, “A simple and low-cost technique for electroless deposition of chalcogenide thin films,” *Semicond. Sci. Technol.*, vol. 9, pp. 1234-1241, 1994.

[59] P. Sampath Kumar and P. Kesavan Nair, “Studies on crystallization of electroless Ni-P deposits,” *J. Mater. Process. Technol.*, vol. 56, pp. 511-520, 1996.

[60] K. Krishnan, S. John, K. Srinivasan, J. Praveen, M. Ganesan, and P. Kavimani, “An overall aspect of electroless Ni-P depositions-A review article,” *Metall. Mater. Trans. A*, vol. 37, pp. 1917-1926, 2006.

[61] L. Ploof, “Electroless nickel composite coatings,” *Adv. Mater. Process.*, vol. 166, pp. 36-38, 2008.

[62] J. N. Balaraju, T. S. N. Sankara Narayanan, and S. K. Seshadri, “Evaluation of the corrosion resistance of electroless Ni-P and Ni-P composite coatings by electrochemical impedance spectroscopy,” *J. Solid State Electrochem.*, vol. 5, pp. 334-338, 2001.

[63] T. R. Tamilarasan, R. Rajendran, M. Siva shankar, U. Sanjith, G. Rajagopal, and J. Sudagar, “Wear and scratch behaviour of electroless Ni-P-nano-TiO_2: Effect of surfactants,” *Wear*, vol. 346, pp. 148-157, 2016.

[64] M. Fang, L. Hu, L. Yang, C. Shi, Y. Wu, and W. Tang, “Electroless plating and growth kinetics of Ni-P alloy film on SiC p / Al composite with high SiC volume fraction,” *Trans. Nonferrous Met. Soc. China*, vol. 26, pp. 799-805, 2016.

[65] H. Wu *et al.*, “Preparation of Ni-P-GO composite coatings and its mechanical properties,”

Surf. Coatings Technol., vol. 272, pp. 25-32, 2015.

[66] Y. S. Dedkov, M. Fonin, and C. Laubschat, “A possible source of spin-polarized electrons: The inert graphene/Ni (111) system,” *Appl. Phys. Lett.*, vol. 92, no. 5, 2008.

[67] W. Gao, “The chemistry of graphene oxide,” *Graphene Oxide Reduct. Recipes, Spectrosc. Appl.*, pp. 61-95, 2015.

[68] J. F. Dai, G. J. Wang, L. Ma, and C. K. Wu, “Surface properties of graphene: Relationship to graphene-polymer composites,” *Rev. Adv. Mater. Sci.*, vol. 40, pp. 60-71, 2015.

[69] T. Ungár, “Strain Broadening Caused by Dislocations,” *Mater. Sci. Forum*, vol. 278, pp. 151-157, 1998.

[70] C. M. P. Kumar, T. V. Venkatesha, and R. Shabadi, “Preparation and corrosion behavior of Ni and Ni-graphene composite coatings,” *Mater. Res. Bull.*, vol. 48, pp. 1477-1483, 2013.

[71] C. Liu, F. Su, and J. Liang, “Producing cobalt-graphene composite coating by pulse electrodeposition with excellent wear and corrosion resistance,” *Appl. Surf. Sci.*, vol. 351, pp. 889-896, 2015.

[72] I. D. S. Bott, L. F. G. Souza, J. C. G. Teixeira, and P. R. Rios, “High-strength steel development for pipelines: A brazilian perspective,” *Metall. Mater. Trans. A*, vol. 36, pp. 443-454, 2005.

[73] M. Gomez, P. Valles, and S. F. Medina, “Evolution of microstructure and precipitation state during thermomechanical processing of a X80 microalloyed steel,” *Mater. Sci. Eng. A*, vol. 528, pp. 4761-4773, 2011.

[74] M. Finsgar and J. Jackson, “Application of corrosion inhibitors for steels in acidic media for the oil and gas industry: A review,” *Corros. Sci.*, vol. 86, pp. 17-41, 2014.

[75] F. Huang, X. G. Li, J. Liu, Y. M. Qu, J. Jia, and C. W. Du, “Hydrogen-induced cracking susceptibility and hydrogen trapping efficiency of different microstructure X80 pipeline steel,” *J. Mater. Sci.*, vol. 46, pp. 715-722, 2011.

[76] C. X. Li and T. Bell, “Corrosion properties of plasma nitrided AISI 410 martensitic

stainless steel in 3.5% NaCl and 1% HCl aqueous solutions," *Corros. Sci.*, 2006.

[77] G. T. B. L.L. Shreir, R.A. Jarman, *Corrosion, Metal/Environment Reactions*. Oxford: Butterworth-Heinemann, 1994.

[78] H. Maleki-Ghaleh *et al.*, "Effect of equal channel angular pressing process on the corrosion behavior of Type 316L stainless steel in Ringer's solution," *Corrosion*, vol. 71, 2015.

[79] Z. Zhu, Z. Liu, and Y. Gu, "Formation of N2 during carbonization of polyacrylonitrile using iron catalyst," *Fuel*, vol. 76, pp. 155-163, 1997.

[80] J. Flis and M. Kuczynska, "Effect of low-temperature plasma nitriding on corrosion of 304L stainless steel in sulfate and chloride solutions," *J. Electrochem. Soc.*, vol. 151, pp. 573-580, 2004.

[81] H. Baba, T. Kodama, and Y. Katada, "Role of nitrogen on the corrosion behavior of austenitic stainless steels," *Corros. Sci.*, vol. 44, pp. 2393-2407, 2002.

[82] H. Baba and Y. Katada, "Effect of nitrogen on crevice corrosion and repassivation behavior of austenitic stainless steel," *Mater. Trans.*, vol. 49, pp. 579-586, 2008.

[83] H. Yashiro, D. Hirayasu, and N. Kumagai, "Effect of Nitrogen Alloying on the Pitting of Type 310 Stainless Steel," *ISIJ Int.*, vol. 42, pp. 1477-1482, 2002.

[84] T. Misawa and H. Tanabe, "High Nitrogen Steels. In-situ Observation of Dynamic Reacting Species at Pit Precursors of Nitrogen-bearing Austenitic Stainless Steels.," *ISIJ Int.*, vol. 36, pp. 787-792, 1996.

[85] Y. Katada, M. Sagara, Y. Kobayashi, and T. Kodama, "Fabrication of High Strength High Nitrogen Stainless Steel with Excellent Corrosion Resistance and Its Mechanical Properties," *Mater. Manuf. Process.*, vol. 19, pp. 19-30, 2004.

[86] H. Baba and Y. Katada, "Effect of nitrogen on crevice corrosion in austenitic stainless steel," *Corros. Sci.*, vol. 48, pp. 2510-2524, 2006.

[87] I. Olefjord and L. Wegrelius, "the Influence of Nitrogen on the Passivation of Stainless Steels," *Corros. Sci.*, vol. 38, pp. 1203-1220, 1996.

[88] X. Yin, L. Hong, and B.-H. Chen, “Role of a Pb2+ stabilizer in the electroless nickel plating system : A theoretical exploration,” *J. Phys. Chem. B*, vol. 108, pp. 10919-10929, 2004.

[89] W. Shao *et al.*, “Graphene oxide reinforced Ni–P coatings for bacterial adhesion inhibition,” *RSC Adv.*, vol. 6, pp. 46270-46277, 2016.

[90] B. T. Lu, J. L. Luo, F. Mohammadi, K. Wang, and X. M. Wan, “Correlation between repassivation kinetics and corrosion rate over a passive surface in flowing slurry,” *Electrochim. Acta*, vol. 53, pp. 7022-7031, 2008.

[91] B. T. Lu, J. L. Luo, H. X. Guo, and L. C. Mao, “Erosion-enhanced corrosion of carbon steel at passive state,” *Corros. Sci.*, vol. 53, pp. 432-440, 2011.

Appendix

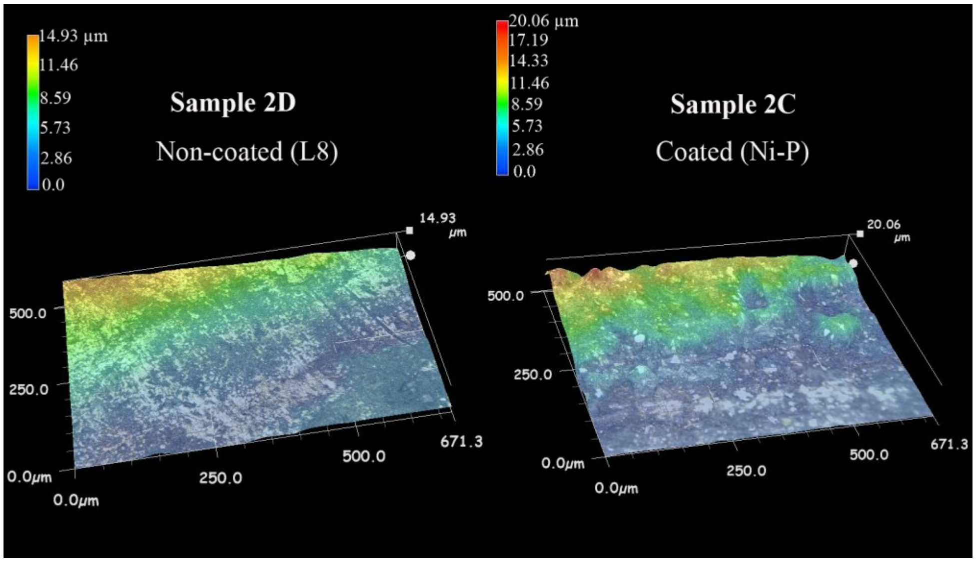

Figure A-1. OSM 3-D image taken from the surface of the coated (2C) and uncoated (2D) samples.

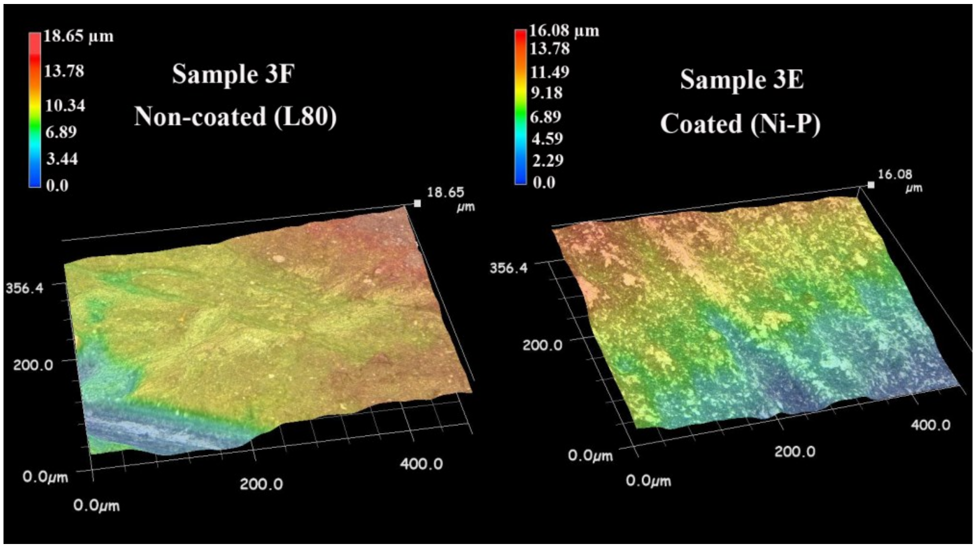

Figure A-2. OSM 3-D image taken from the surface of the coated (3E) and uncoated (3F) samples.

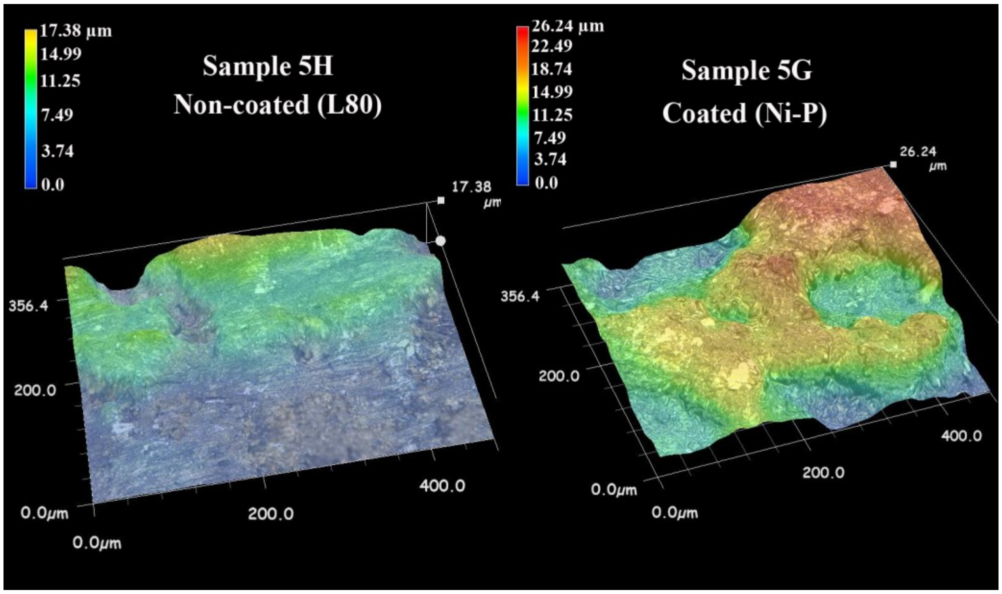

Figure A-3. OSM 3-D image taken from the surface of the coated (5G) and uncoated (5H) samples.

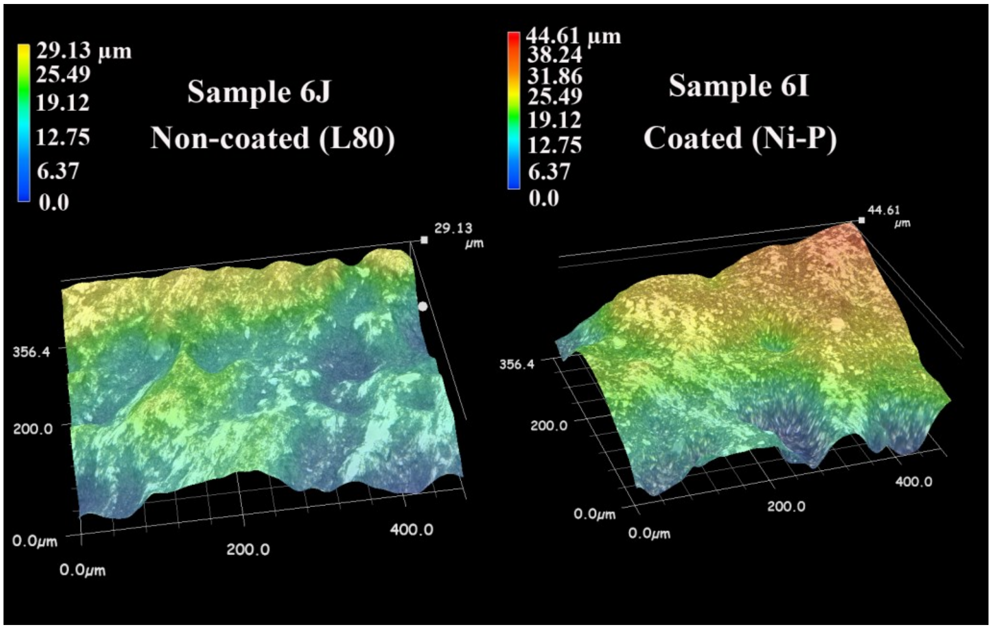

Figure A-4. OSM 3-D image taken from the surface of the coated (5G) and uncoated (5H) samples.

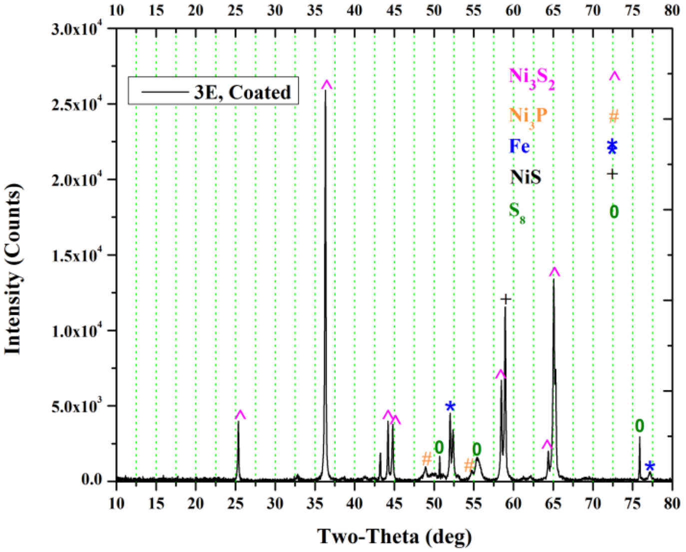

Figure A-5. X-ray diffraction patterns of the sample 3E.

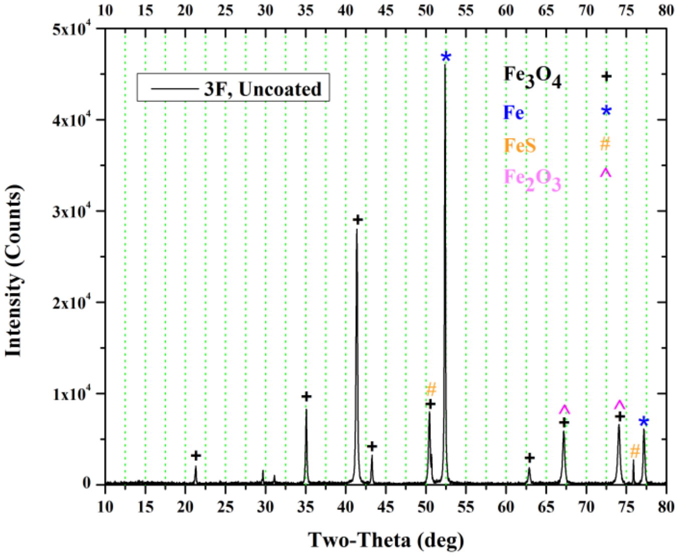

Figure A-6. X-ray diffraction patterns of the sample 3F.

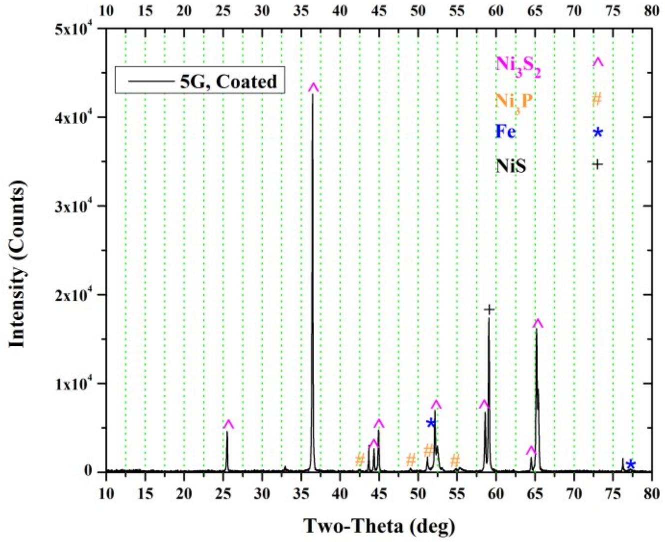

Figure A-7. X-ray diffraction patterns of the sample 5G.

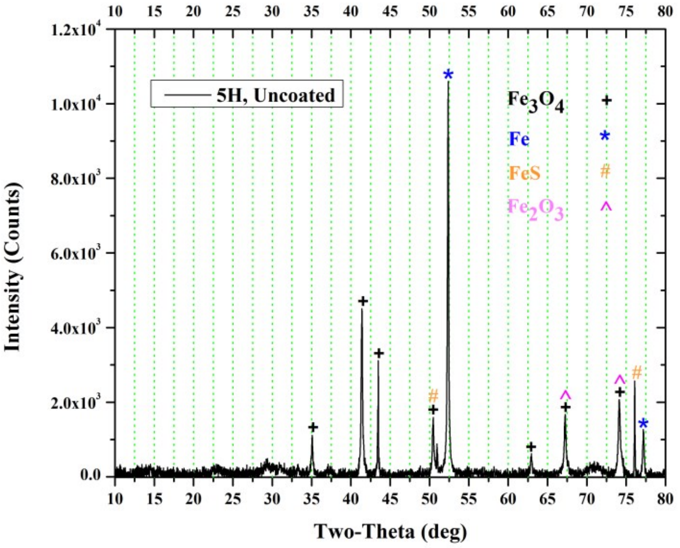

Figure A-8. X-ray diffraction patterns of the sample 5H.

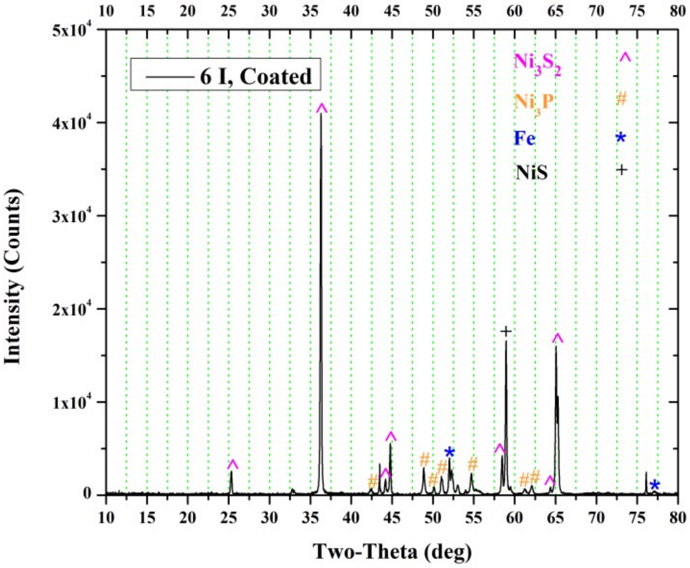

Figure A-9. X-ray diffraction patterns of the sample 6I.

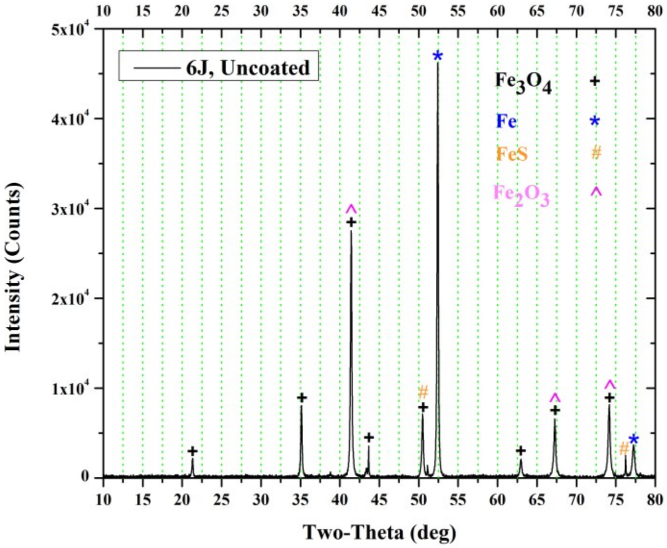

Figure A-10. X-ray diffraction patterns of the sample 6J.